

Automated Disease Identification With 3-D Optical Imaging: A Medical Diagnostic Tool

This paper provides an overview of the development of compact digital holographic microscopes and their applications in 3-D cell imaging, cell parameter extraction, and cell classification for potential automated disease identification.

BY ARUN ANAND, INKYU MOON, *Member IEEE*, AND BAHRAM JAVIDI, *Fellow IEEE*

ABSTRACT | Digital holographic microscopy is an ideal tool for 3-D cell imaging and characterization. It provides a host of cell parameters based on cell morphology and its temporal dynamics or time variation. These parameters can be used to study and quantify cell growth and cell physiology. When coupled with classification algorithms, this technique can also be used to identify and classify cells such as blood cells for automated disease identification. A compact, portable version of this 3-D optical imaging system has the potential to become a device for compact field portable biological data collection, analysis, and cell identification leading to disease diagnosis with mobile devices, low cost instruments for deployment in remote areas with limited access to healthcare to combat disease. In this paper, we present an overview of our reported work on the development of digital holographic microscopes and their applications in 3-D cell imaging, cell parameter extraction and cell classification for potential automated disease identification.

KEYWORDS | Biological cells; biomedical imaging; cell identification; cellular biophysics; classification algorithms; holography; medical diagnostic imaging; microscopy

I. INTRODUCTION

Imaging, visualization, quantification and identification of cells and tissue is an interesting and challenging problem in all areas of life sciences. Cells are the basic and functional units of life in all living things, from microorganisms to humans. They host the biological machinery that makes the proteins, chemicals and signals responsible for everything happening inside our bodies. Investigating these structural elements is essential in understanding their function. Measurements and analysis of the components of cells and their physiology are vital in the diagnosis of diseases such as cancer. In particular, study and diagnosis of diseases greatly benefit from the development of exotic imaging techniques that can provide information on cell characteristics without the need for labelling. Increasing demand for accurate early diagnosis and treatment of diseases are the major factors fuelling the growth of medical diagnostics and medical therapeutics. Cellular imaging still remains one of the most sought-after techniques to achieve this.

Optical microscopes are one of the most widely used instruments in cell imaging and cell studies [1], [2]. Conventional microscopes cannot provide the direct measurement of spatial phase or optical path length (OPL) and index of refraction of cells, which makes it difficult to quantify cell parameters.

Manuscript received August 17, 2016; revised October 03, 2016; accepted November 29, 2016. Date of publication March 16, 2017; date of current version April 20, 2017. This work was supported by a research grant from DAE-BRNS (2013/34/11/BRNS/504), Government of India, and by the Basic Science Research Program through the National Research Foundation of Korea, which is funded by the Ministry of Science, ICT & Future Planning (NRF-2015K1A1A2029224). The work of B. Javidi was supported by the National Science Foundation (NSF) under Grant NSF/IIS-1422179 and Grant NSF ECCS 1545687.

A. Anand is with the Optics Laboratory, Applied Physics Department, Faculty of Technology and Engineering, The M. S. University of Baroda, Vadodara 390001, India (e-mail: aanand-apphy@msubaroda.ac.in).

I. Moon is with the Department of Computer Engineering, Chosun University, Gwangju 501-759, South Korea (e-mail: inkyu.moon@chosun.ac.kr).

B. Javidi is with the Department of Electrical and Computer Engineering, University of Connecticut, Storrs, CT 06269-4157 USA (e-mail: bahram@engr.uconn.edu).

Interference and digital holographic microscopy have the ability to provide direct measurement of the biophysical parameters such as optical path difference (OPD) and index of refraction based on the interference between the light beams passing through the specimen and a reference beam [1]–[3] from a single interference pattern [4] as well as temporal fluctuations of live cells. With digital holographic microscopes, quantitative images of cells can be reconstructed, allowing researchers to generate detailed, label-free 3-D structures of cells. In the field of holography [5] and interferometry, advances in cost effective lasers, compact data acquisition equipment, as well as computing technologies, have led to the development of effective digital holographic microscopes leading to reliable, automated and low-cost tools for rapid sensing, imaging and identification of biological specimens, which can be used to detect and track various biological activities [6]–[60].

Digital holographic microscopes integrated with numerical processing such as image processing, statistical pattern recognition and machine learning algorithms allow researchers to investigate, detect and identify biological cells, processes, contexts or responses of various biological specimens in noninvasive, real-time conditions [8]–[12], [14]–[18], [35], [40], [41], [49]. Although it is difficult to extract quantitative phase information directly from a single in-line hologram, simplified digital holographic microscopes have been studied for identification and tracking of biological specimens with large advantages in simplicity, compactness and low cost [8]–[19]. The fusion of digital holography and information processing bears promise for a reliable and automated instrument, which can be efficiently used in the field of cell biology [8]–[18]. On the other hand, digital holographic quantitative phase microscopy (DH-QPM) with off-axis configurations can efficiently extract information about the index of refraction and thickness of biological specimens from a single hologram [20]–[60]. This can provide reliable quantitative phase mapping of the observed specimen with nanometer axial sensitivity. Therefore, DH-QPM enables researchers to obtain rich, noninvasive quantitative biophysical information about the structure of cells and microorganisms such as blood cells, cardiomyocyte, protozoa, nerve cells, embryonic stem cells, cancer cells and even tissue [26], [30]–[32], [36]–[38], [40]–[60]. Also, DH-QPM can aid researchers in the analysis of cell dynamics (or temporal fluctuations), cell division, as well as biological activities at different time scales ranging from a few milliseconds to several days [26], [31], [32], [35]–[38], [46], [47], [50]–[60]. Another advantage of DH-QPM is that images can be captured of both single cells and populations.

In this paper, we provide an overview of our work in the development of different classes of 3-D imaging instruments such as digital holographic systems for 3-D cell imaging and cell dynamics (temporal fluctuations) measurements, cell parameter extraction for automated cell classification and their potential applications to disease identification with 3-D optical imaging approaches. Fig. 1 illustrates an example of

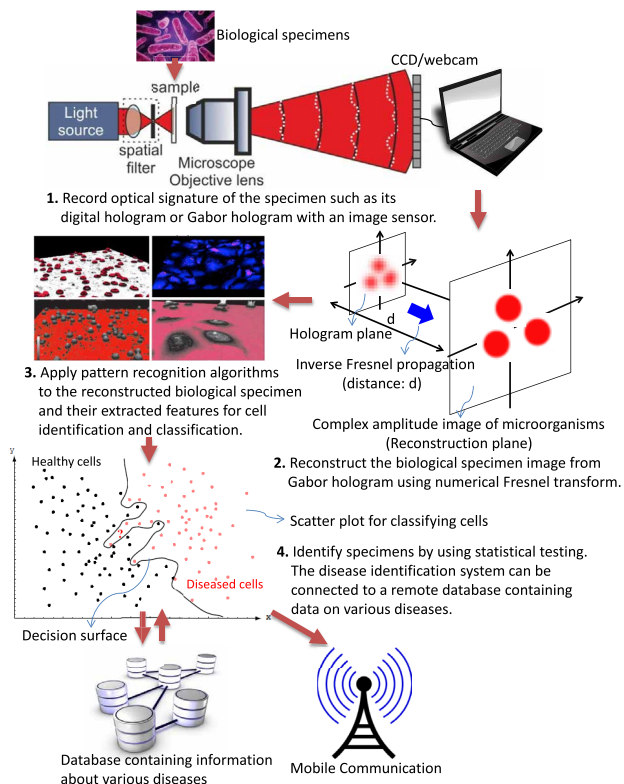


Fig. 1. Block diagram for 3-D sensing and identification of biological microorganisms such as blood cells using DHM interfaced with a mobile device such as a laptop and connected to a remote database containing reference data for disease identification [10], [12], [14], [15]. The light source can be compact and inexpensive such as an incoherent source or a laser diode [12].

our approach for automated 3-D optical sensing and imaging for identification of biological microorganisms such as blood cells using digital holographic microscopy for disease identification. The biophotonics sensor may be interfaced with a mobile device such as a laptop and connected to a remote database containing reference data for disease identification [10], [12], [14], [15]. The light source can be compact and inexpensive such as an incoherent source [12] or a low-cost laser pointer or a partially coherent source such as band-pass filtered white light source. The optical sensor can be made to be compact and stable for a field portable low-cost system for automated disease identification.

The paper is organized as follows. Section II explains the basic concept of the digital holographic microscopy. Sections III and IV explain on-axis digital holographic microscope and Gabor digital holographic microscope. In Section V we present off-axis digital holographic microscopy applied to cell imaging analysis, and identification. The self-referencing digital holographic microscopy applied to cell identification is described in Section VI. Measurements of the temporal dynamics of the cells is presented in Sections V–VI. Finally, the conclusion is presented in Section VII.

II. DIGITAL HOLOGRAPHIC MICROSCOPY

Three-dimensional imaging of micro-objects can be achieved by employing interferometric methods. Quantitative phase microscopy techniques using interference principle provides high contrast images of cells, which are mostly transparent to visible light, along with the thickness information about the object [4]. Digital holography is an interference-based technique providing information on the 3-D features of an object. It works by optically recording holograms (interference patterns) on digital arrays and numerically reconstructing them in a computer by simulating the diffraction of light field from the recorded holograms to yield the complex amplitude information (phase and amplitude) of the wavefront [4], [61], [62]. From the reconstructed complex amplitude distribution spatial phase variation of the object can be extracted and used to estimate its thickness profile [4]. Another advantage of numerical reconstruction is that it can provide information at different object layers numerically (numerical focusing), without the need for mechanical scanning [62]. The recording of the hologram is a single-shot process and the reconstruction provides the thickness information of the whole cell from a single hologram. These features make digital holography an attractive tool for noninvasive, real-time 3-D imaging as well as identification of microorganisms.

A. Basics of Digital Holographic Microscope

As mentioned in the previous paragraph, digital holography is an interferometric technique, meaning it involves the superposition of at least two wavefronts. In digital holographic microscopy, the magnified object beam (light beam modulated by the object) is made to superpose with a known background known as the reference beam (light beam not modulated by object) as shown in Fig. 2. Object and reference beam superpose at the pixilated digital array to form the holograms. If the complex amplitude distributions of the object and reference beam at the hologram plane are $U_O(x, y) = O(x, y) e^{-i\varphi_O(x, y)}$ and $U_R(x, y) = R(x, y) e^{-i\varphi_R(x, y)}$ respectively (where O and R are the scalar amplitude distributions and φ_O and φ_R are the phase distributions), intensity profile, $I(x, y)$, of the hologram sampled by the digital sensor can be written as [61]

$$I_T = I_O + I_R + RO * e^{i(\varphi_O - \varphi_R)} + R * O e^{-i(\varphi_O - \varphi_R)} \quad (1)$$

where I_O and I_R are the intensity of the object and reference beam respectively and ‘*’ represents complex conjugation. Equation (1) tells us that the object phase information is encoded as the modulation of the interference pattern (hologram) [20]–[54].

A separate reference beam unmodulated by object information is not always necessary for the formation of the hologram. In the case of Gabor holography, the object is kept in the path of the light beam and the portion of

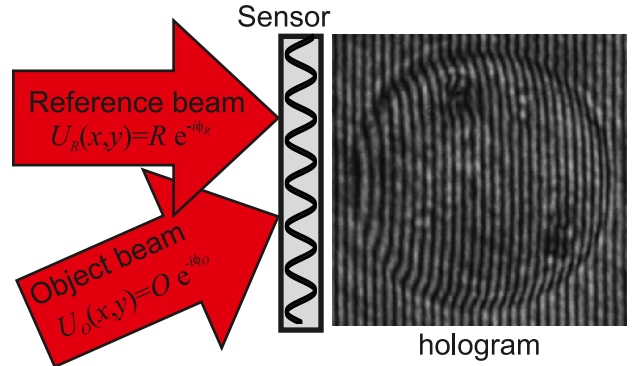


Fig. 2. Formation of hologram in digital holographic microscope.

the beam scattered from the object interferes with the portion of the beam which is not scattered [5], [7], [9], [10], [12]–[19]. In the case of self-referencing digital holographic microscopy (SRDHM), a portion of the object wavefront unmodulated by object information is made to interfere with the portion carrying object information to create the holograms [55]–[60].

B. Reconstruction of Digital Holograms

In holography, reconstruction of the image is obtained from the scattered reference beam shined on the microstructures of the hologram and in digital holography reconstruction is done numerically by shining the exact digital replica of the reference beam on the hologram [Fig. 3], which is equivalent to [62]

$$I_T R e^{-i\varphi_R} = (I_O + I_R) R e^{-i\varphi_R} + R e^{-i\varphi_R} R O * e^{i(\varphi_O - \varphi_R)} + R e^{-i\varphi_R} R * O e^{-i(\varphi_O - \varphi_R)}. \quad (2)$$

In (2), the first term represents the undiffracted reference beam, second and third terms provide information about the distorted real image and the virtual image, respectively.

The complex amplitude of the object at the image plane is obtained by simulating the propagation of the scattered reference beam from the structures of the hologram by numerical implementation of scalar diffraction integral [63] as shown in Fig. 3.

The numerical propagation process can be based on Fresnel–Kirchhoff diffraction integral or the angular spectrum approach towards the diffraction theory [63]. Both these integrals describe the propagation of the reconstructing wave from the hologram plane to the image plane. For propagation distances much larger than the size of the hologram, Fresnel–Kirchhoff integral with Fresnel approximation is the appropriate approach for numerical propagation. In the case of digital holographic microscopy, where the distance between the hologram and the image planes are very small, the angular spectrum approach will be useful as it describes the wavefront propagation over short distances. The hologram

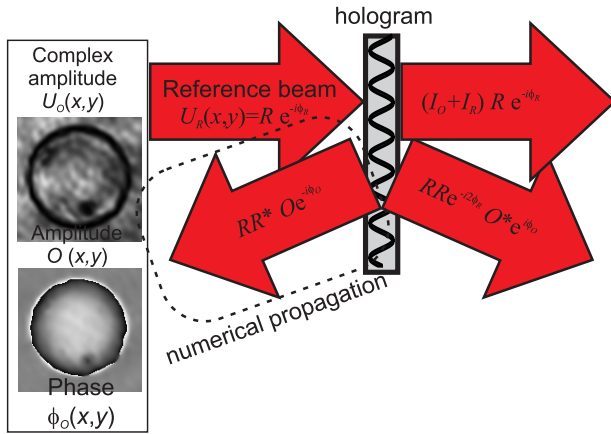


Fig. 3. Reconstruction of digital hologram.

plane is usually at the image plane of the lens magnifying the object, making the numerical reconstructions faster.

C. Computation of Intensity and Phase

Numerical reconstruction of digital holograms provides the complex amplitude distribution $U_O(x, y)$ of the object wavefront at the image plane. From the complex amplitude the intensity and phase of the object at the image plane can be computed. The intensity of the object wavefront is given by [62]

$$I(x,y) = |U_O(x,y)|^2. \quad (3)$$

Phase of the object wavefront is given by

$$\varphi_O(x,y) = \arctan \frac{\text{Im}[U_O(x,y)]}{\text{Re}[U_O(x,y)]}. \quad (4)$$

In order to compensate for the aberrations due to optical elements two holograms are recorded for each object. One is recorded with the object in the field of view and is called the object hologram and the second one is recorded with the medium surrounding the object in the field and is called the background hologram. These holograms are reconstructed individually and the subtraction of the background hologram phase from the object hologram provides the phase difference distribution $\Delta\varphi(x, y)$, nullifying the phase change introduced by the optical elements, which remained the same between the exposures. The phase difference is related to the object thickness $h(x, y)$ through

$$\Delta\varphi(x,y) = \frac{2\pi}{\lambda} (n_O - n_B) h(x,y) \quad (5)$$

where λ is the vacuum wavelength of the source, n_O and n_B are the constant average refractive indices of the object and the surrounding medium, respectively. If the refractive indices of the object and the surrounding medium are known, the thickness profile of the object can be computed otherwise the phase difference can be used to compute the optical thickness profile ($n \times h$) of the object. Optical thickness profile also carries enough information for object characterization and identification.

III. ON AXIS DIGITAL HOLOGRAPHIC MICROSCOPE

In this section, we overview single-exposure online (SEOL) digital holographic microscopy integrated with statistical sampling methods for automated 3-D imaging and recognition of biological specimens [8]–[12], [14]–[18] which was first proposed for cell identification [8]. For 3-D imaging of biological specimens, a coherent beam propagates through the specimen and its diffraction pattern by the microscope objective is interfered with by the reference beam on the image sensor. The image sensor interfaced with a computer optically records the interference pattern. In this configuration, separate object and reference beams travel parallel to each other and interfere (see Fig. 4).

The interference pattern or SEOL digital hologram recorded at the image sensor plane or hologram plane is represented by (1). The first term in (1) can be dropped on the condition that the SEOL holograms for more dense specimens are recorded because $I_O \ll I_R$ and the second term can be assumed as a constant or easily removed by high-pass filtering. With the conjugate component of the SEOL digital hologram, it is demonstrated that crosstalk between real and conjugate terms are bound to low spatial frequencies in the SEOL digital holographic microscope [14]. Also, it is shown that the conjugate component in the single-exposure on-line digital holographic microscope can be neglected if many fringe patterns of the biological specimen are captured by the CCD detector. Because of this condition, it can be assumed that the original focused image from the single-exposure on-line digital hologram is strongly dominant, whereas the defocused twin image overlapping the focused image is much weaker. Therefore, the field distribution of the original biological specimen from the single-exposure on-line digital hologram pattern can be calculated numerically by the following inverse Fresnel transformation or angular spectrum method with two Fourier transforms, which cancels the scale factor between the input and output [21], [22], [24], [64]

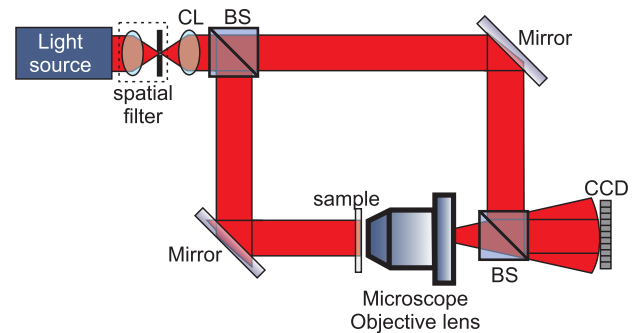


Fig. 4. Experimental setup for recording the SEOL digital hologram of biological specimens. BS - beam-splitter, CL - collimating lens.

$$O(x',y') = \text{IFrT}\{I(x,y)\} \\ = \text{IFT}\left(\text{FT}\{I(x,y)\} \times \exp\left\{j\pi\lambda d_0 \left[\frac{u^2}{(\Delta x N_x)^2} + \frac{v^2}{(\Delta y N_y)^2}\right]\right\}\right) \quad (6)$$

where (x',y') are the object plane coordinates and d_0 is reconstruction distance, u and v denote transverse discrete spatial frequencies, $(\Delta x, \Delta y)$ is resolution at the hologram plane, and N_x and N_y are the whole hologram size in the x , y direction, respectively. Therefore, many wavefronts at arbitrary depth along the z -axis, including the one representing the biological specimen in focus, are computed from a single SEOL digital hologram. As an additional merit, the single-exposure on-line digital holographic microscope allows one to obtain a dynamic time-varying scene digitally restored on the computer for monitoring and recognizing moving and growing micro/nano biological organisms since it can be robust to external noise factors such as fluctuation and vibration. Moreover, object distributions need not be sparse in the single-exposure on-line digital holographic microscope because the reference-to-object wave ratio can be controlled by the user [19].

IV. GABOR DIGITAL HOLOGRAPHIC MICROSCOPE

In single-exposure on-line DHM, the digital Fresnel holograms from specimens are recorded in on-axis configurations. The major advantage in on-axis configuration with no angular separation between the two interfering beams is that the user can control the reference-to-object beam ratio, which allows for optimal recording of the digital holograms of more dense objects [19]. If the specimens are relatively thin and transparent, however, the single-exposure on-line digital holographic microscope can be much simpler to implement. This mode is referred to as the Gabor digital holographic microscope, and it allows for the use of inexpensive partially coherent light sources or band-pass filtered white light illuminations instead of a fully coherent source such as gas lasers owing to the fact that the unscattered beams or photons passing through the specimen and its surrounding medium provide the necessary reference beam for recording of hologram patterns [5], [10], [12]–[15]. In Gabor DHM, the two arms of on-axis or off-axis configurations can be collapsed into one path (see Fig. 5). After recording the Gabor holograms of specimens, Fresnel transformation or angular spectrum approaches defined in (2) can be used for computational reconstruction of specimens. Involvement of informational processing algorithms such as statistical pattern recognition, computer vision and machine learning algorithms can be further extended for recognition and classification of biological micro/nano-organisms, as well as for tracking them in 3-D space with the reconstructed holographic images of the specimens [8].

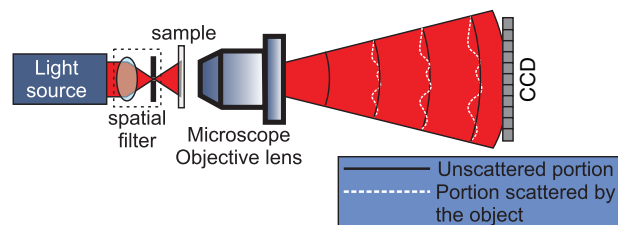


Fig. 5. Experimental setup for recording the Gabor digital hologram of biological specimens. A portion of the wavefront not scattered by the object (reference wavefront) interferes with portion of the wavefront scattered by the object (object wavefront), resulting in the formation of holograms. Here short coherent sources also produce good contrast interference fringes, since the path length difference between the beams is due to the object alone.

V. OFF-AXIS DIGITAL HOLOGRAPHIC MICROSCOPY APPLIED TO CELL IMAGING AND IDENTIFICATION

Digital holographic microscopes work on the principle of superposition of object beam with a reference beam. In Gabor holography, the reference beam was the nonscattered portion of the wavefront illuminating the object. As can be seen from (2), in this geometry the virtual and real images are not spatially separated and it becomes difficult to extract the correct object phase distribution. In the single-exposure on-line digital holographic microscope since the reference beam is in line with the object beam, phase shifting is required to obtain phase information. To overcome these hurdles a separate reference beam is introduced at an angle with the object beam to create off-axis geometry (like the one shown in Fig. 1) [20]–[53]. This leads to spatial separation of the three terms in (2) at the image plane, eliminating the twin image problem and making it possible to extract the object phase information from a single hologram.

In this section, we present an overview of the automated quantitative analysis of red blood cells (RBCs) and cardiomyocytes (cardio cells) to demonstrate that the imaging informatics coupled to digital holographic microscope has very high potential in the area of cell biology [38], [40], [41], [45], [47]–[49].

One of the most commonly employed digital holographic microscope geometries for investigating biological objects in the transmission mode uses the Mach–Zehnder interferometer configuration as shown in Fig. 6, to create off-axis DH-QPM [20]–[43], [45]–[49], [51], [53]. One of the beams from a laser source split into two by a beam splitter transilluminates the object and acts as the object beam. It is made to interfere with the second beam (reference) at an angle resulting in the creation of off-axis holograms. Usually laser sources working in the red region of visible spectrum (632.8 nm in the case of He–Ne lasers and 635 nm in the case of laser diode module) are preferred. They are easily available and

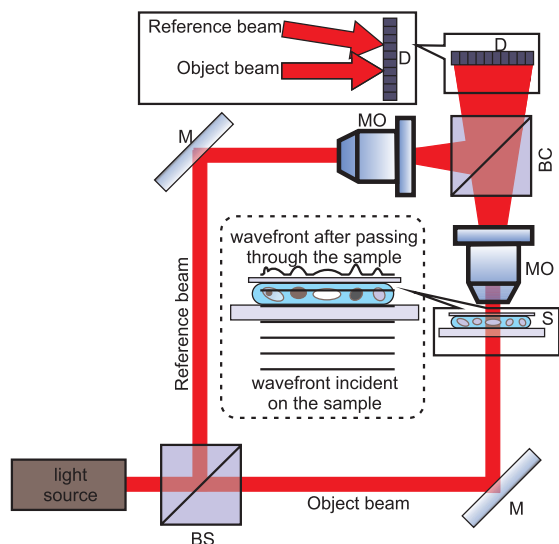


Fig. 6. Off-axis digital holographic microscope employing Mach-Zehnder interferometer geometry. BS – beam splitter, M – mirror, S – sample, MO – microscope objective lens, BC – beam combiner, D – digital array. Inset shows that the object and reference beam interfering at an angle.

are absorbed less by living cells, compared to shorter wavelengths [65]. Low temporal coherent sources can also be used as the light source, but it requires special optical elements for matching of the path lengths so as to achieve high contrast interference fringes [39], [50], [51]. The field of view is also limited by the spatial coherence of the source [50].

A. Automated RBC Analysis

Blood consists of different types of cells but RBCs or erythrocytes are the most abundant ones. The RBC's shape is optimum for maximal deformation, the maximum surface at a given volume, rapid changes and survival of the cell during its many repeated passages through the narrow channels. These conditions are satisfied by a biconcave disk shape, which is considered the norm for the RBCs (Fig. 7). The RBC has a

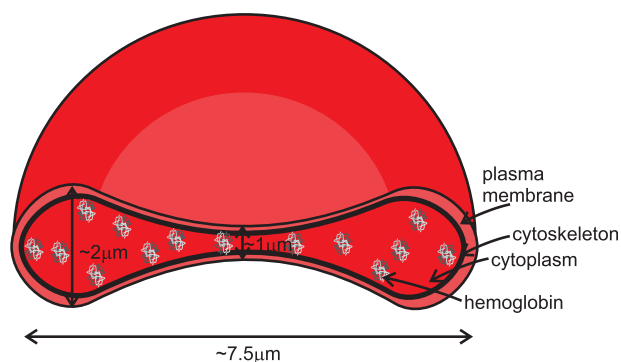


Fig. 7. Structure of human red blood cell.

flexible membrane with a high surface-area-to-volume ratio (SVR) that facilitates large reversible elastic deformation of the RBC as it repeatedly passes through small capillaries during microcirculation. The RBC membrane, vital to the shape and function of RBC, consists of a lipid bilayer and an internal cytoskeleton supporting the lipid bilayer. Hemoglobin is the most important component of red blood cells and constitutes about 33% of the cytoplasm. It has been discovered that the loss of membrane function is most likely related to some abnormality in the maintenance of the cytoskeleton of RBC and shape changes of the membrane [66], [67].

Fig. 8(a) shows the hologram of a healthy human red blood cell recorded with off-axis digital holographic microscope. A background hologram, with the surrounding medium (blood plasma) present in the field of view is also recorded for phase compensations [Fig. 8(b)]. These holograms are reconstructed using numerical implementation of angular spectrum propagation integral [63], to retrieve the complex amplitude information at the image plane. Fig. 8(c) shows the reconstructed intensity at the image plane after numerical focusing. The intensity profile provides only limited information about the object and has low contrast as most of the beam is transmitted through the cell. The retrieved quantitative phase contrast profile of the cell is shown in Fig. 8(d), which has higher contrast and higher information content compared to the intensity profile. The phase profile is used to compute the thickness profile of the cell using (5), using constant average refractive index values of 1.42 for the red blood cell and 1.34 for the plasma [68] and is shown in Fig. 8(e). The cross sectional thickness profile of the cell is shown in Fig. 8(f). The bi-concave shape of the RBC can be seen from these figures. Fig. 8(d)–(f) shows the potential of the technique for high contrast quantitative phase imaging of cells. The cell morphology obtained from quantitative phase images (QPIs) is used for cell visualization as well to extract the physical, optical and mechanical parameters of the cells, which in turn is used for cell classification [14], [25], [32].

In the case of RBC, it is shown that 3-D morphological parameters related to its shape profile including mean corpuscular hemoglobin (MCH) and MCH surface density (MCHSD) of normal RBCs can be obtained by the off-axis digital holographic microscope to identify various types of RBCs. By monitoring MCH, for example, any modifications or conservation of the hemoglobin content in RBCs can be investigated since the phase of an optical beam is directly related to the MCH [69]. The ability of DH-QPM in studying RBC parameter is not limited only to MCH and MCHSD. Projected area (PA), average phase value within the RBC area and sphericity coefficient can also be calculated from QPIs provided by the DH-QPM technique. The normal RBC can undergo various shape transitions. The most common types are biconcave, stomatocyte, and echinocyte RBCs. Theoretical considerations can provide explanations about the echinocyte shape transitions of RBCs [70]. However, their mechanical changes in blood diseases have not been studied

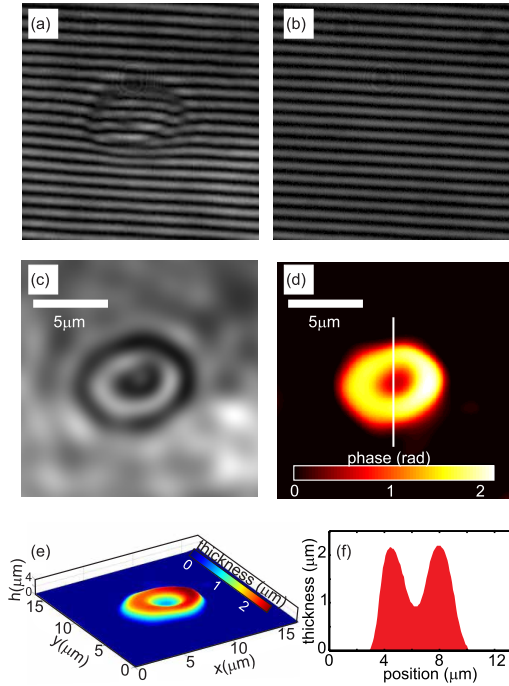


Fig. 8. Quantitative phase imaging using two-beam off-axis DHM. (a) Recorded hologram of a human red blood cell using a microscope objective lens (MO) of 40X magnification and NA of 0.65. A random linearly polarized laser source working at 632.8 nm was used along with an 8-bit CCD camera with 4.65- μm pixel pitch to record the holograms. (b) Hologram of the background (blood plasma). (c) Intensity profile of the blood cell at the image plane obtained by numerical focusing. (d) Quantitative phase image of the red blood cell. (e) Thickness profile of the RBC computed using the phase distribution. (f) Cross-sectional thickness profile of the RBC.

quantitatively and statically. We experimentally show that joint statistical distributions of the characteristic parameters of RBCs obtained from QPIs can be used as feature patterns.

B. Automated Quantitative RBC Analysis at Single-Cell Level

To isolate single RBCs, marker-controlled watershed segmentation algorithm is applied to the images [42]. A simple thresholding with the background phase information can also be used for this [38]. For investigating the characteristic properties such as 3-D morphology and MCH of RBCs, PA and mean of phase values of single RBCs are automatically measured. PA and mean of phase values are computed from the following equations, respectively [41], [43]:

$$S = N \frac{p^2}{M^2}, \quad \bar{\varphi} = \frac{1}{N} \sum_{i=1}^N \varphi_i \quad (7)$$

where N denotes the total number of pixels within the single RBC, p denotes the pixel size, M is the lateral magnification of the microscope and φ_i is the phase value at the i th pixel within the single RBC with the phase value of the

background set to zero. In this study pixel size is 0.159 μm . The sphericity coefficient of k can be obtained by dividing the thickness at the center of the RBC by the thickness at a quarter of its diameter. The sphericity coefficient k as a morphological measurement is defined as follows [41]:

$$k = ph_c / ph_d \quad (8)$$

where ph_c and ph_d are phase values at the center of the RBC and at a quarter of its diameter, respectively. A value close to unity indicates that the RBC has a shape close to a sphere (echinocyte). In contrast, a value smaller than unity tells that the shape is closer to that of a doughnut. Another important property is the dry mass or MCH value and it is the mass of the RBC when it is completely dried. The following equation provides the MCH of the RBC [41]:

$$\text{MCH} = \frac{10\lambda}{2\pi\alpha} \int_S \varphi ds = \frac{10\lambda}{2\pi\alpha} \bar{\varphi} S \quad (9)$$

where λ is the wavelength of the light source, φ is the phase value of each pixel within a RBC, α is the refractive increment (in m^3/kg or dl/g) related to the protein concentration. MCH is an important parameter which can be used to investigate any distinctions, alterations or conservation of the hemoglobin content in RBCs. The MCHSD for the measurement of the MCH concentration can be calculated from dividing the MCH by the PA as [41]

$$\text{MCHSD} = \text{MCH}/\text{PA}. \quad (10)$$

Fig. 9 shows the phase images of two RBC samples recorded using two-beam off-axis DH-QPM. In Fig. 9(a) stomatocyte RBCs are predominant while in Fig. 9(b) discocyte RBCs are predominant. These two samples are used for the automated quantification of 3-D morphology, MCH, and MCHSD of RBCs.

We take advantage of using the marker-controlled watershed segmentation algorithm not only by the segmenting the image but also by labelling each single RBC. Having counted pixels, then, PA of each RBC can be calculated by (7). Since the inner region of RBC has a different shape depending upon the type of RBC, the inner and outer part of RBC can be examined separately (see Fig. 10).

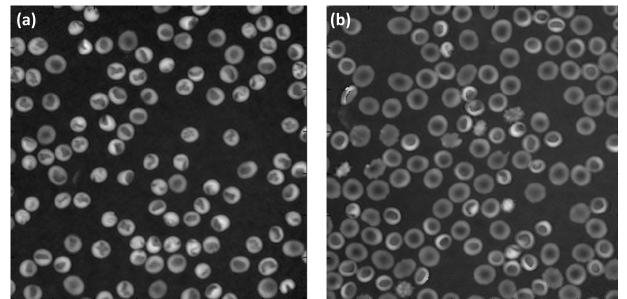


Fig. 9. Reconstructed phase images of RBC. (a) RBCs with predominantly stomatocyte shape. (b) RBCs with predominantly discocyte shape [41].

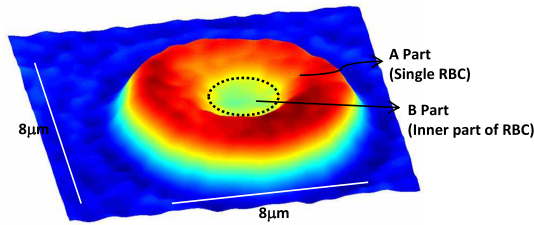


Fig. 10. Different parts in the red blood cells [49].

Part B, which is located on the interior of the part A, is the region of lower phase than part A, resulting from the biconcave shape of RBCs.

Fig. 11 shows the statistical distributions of PA (X_1), and the mean of the phase value (X_2) in the A part of RBC (see Fig. 10). The mean and standard deviation of RBCs with a stomatocyte shape for X_1 are $34 \mu\text{m}^2$ and $5 \mu\text{m}^2$, respectively, and are 97° and 9° for X_2 , respectively. In contrast, for a discocyte RBC, the mean and standard deviation of variable X_1 are $42 \mu\text{m}^2$ and $8 \mu\text{m}^2$, respectively, and are 74° and 15° for variable X_2 , respectively. It is worth mentioning that the stomatocyte RBCs tend to be more similar to each other than discocyte RBCs since stomatocytes are inclined to be much closer to the mean value. In the case of the mean of the phase value in the A part, stomatocyte RBCs are larger than the discocyte RBCs while the mean PA in the A part of stomatocyte RBCs is smaller than discocyte RBCs. It should be mentioned that there is a 23° difference between the average phase values in the A part of the RBCs with the different types of shapes. Regarding the average PA value in the A part of different RBC, a difference of approximately $8 \mu\text{m}^2$ has been observed. Also, the overlapped area between two statistical distributions states that average phase value has stronger ability to discriminate two categories of RBCs than PSA variable.

Experiments also revealed that PA for the inner part (B) is $10 \mu\text{m}^2 \pm 5 \mu\text{m}^2$ (mean \pm std), and the mean phase value (MPV) is $81^\circ \pm 12^\circ$ in RBCs with the stomatocyte shape. In contrast, PA in discocytes in the part B is $18 \mu\text{m}^2 \pm 5 \mu\text{m}^2$, and those for MPV are $60^\circ \pm 11^\circ$, respectively. The PA in the B part of the stomatocyte RBCs is about $8 \mu\text{m}^2$ smaller than the corresponding value in the discocyte type while the standard deviation is very similar. Fig. 12 shows the scatter plot of stomatocyte and discocyte RBCs according to the two variables of PA and mean phase value in A and B parts, where many single RBCs from the phase images of RBCs having the different shapes were investigated. As shown in Fig. 12, the projected area of the A or B parts is inversely proportional to the mean phase value in the A or B parts of both types of single RBCs. Furthermore, there is a strong correlation between projected area and mean phase value in the A or B parts of both types of single RBCs.

MCH value for stomatocyte RBCs is 31.1 ± 4.0 pg, while MCH for discocyte type is 28.9 ± 4.0 pg. These averaged MCH values for both types of RBCs are approximately in the

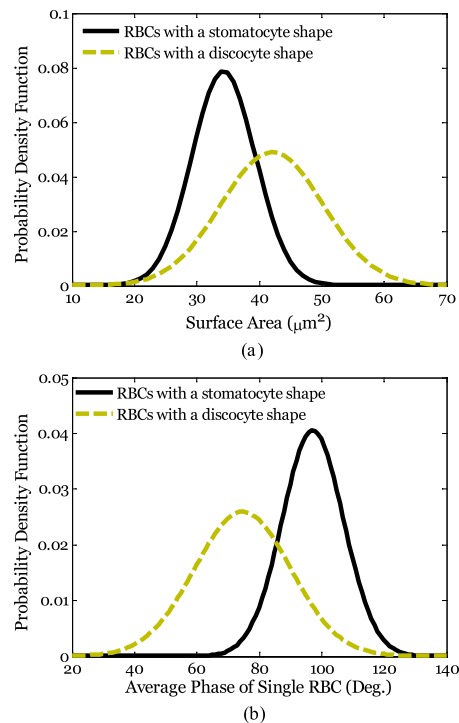


Fig. 11. (a) Two statistical distributions for the projected area (PA) of RBCs. (b) Two statistical distributions of the mean of phase value in the RBC area. The solid line is for the RBCs with a stomatocyte shape. Dotted line is for the RBCs with a discocyte shape [41].

typical range of [27], [31] picogram/cell. Fig. 13(a) shows the statistical distributions of the MCH in the A part of a single RBC where we have computed the MCH of RBCs with the different types of shapes [71]. Note that the MCH of RBCs with a stomatocyte shape is a little larger than RBCs with a discocyte shape. Fig. 13(b) shows the scatter plot of the two categories of RBCs by two variables of MCH and MCHSD. Sphericity coefficient as previously mentioned can explain the similarity of an RBC to a spherocyte RBC. The sphericity coefficient in RBCs with a stomatocyte shape is calculated to be 0.54 ± 0.21 , while this value RBCs with a discocyte shape is 0.63 ± 0.18 .

C. Cell Morphology-Based Classification of RBCs Using Holographic Imaging Informatics

A robust classification strategy is essential to analyze RBCs for medical diagnosis and therapeutics. In addition, an RBC classification algorithm would be helpful in screening RBC-related drugs or agents. We believe that using conventional 2-D imaging systems for quantitative analysis of RBCs is limited because they cannot provide important biophysical cell parameters related to the structure and shape of RBCs. Therefore, development of an RBC classification method based on quantitative holographic imaging with greater efficiency and accuracy

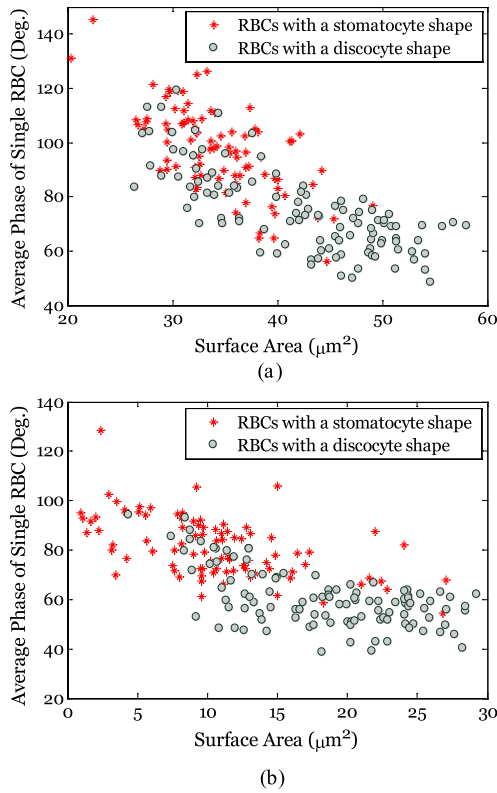


Fig. 12. Scatter plot of the relationship between the projected area and the mean of the phase value for (a) A part and (b) B part (see Fig. 10) in the single RBC [41].

is imperative. In this section, we overview automated methods to classify RBCs by analyzing the equality of the covariance matrices in features-extracted RBC holographic images [49]. Our simulation results demonstrate that the morphological or geometrical features of RBC can be useful in RBC classification.

At first, the Gabor wavelet filter is applied at the single-RBC level [72]. This filter is the optimal compromise between spatial resolution and frequency resolution. Also, it has good noise tolerance according to its band-limited property and the representation of the local features centered on feature points by its coefficients. The continuous wavelet transformation of the extracted RBCs is then defined as [10]

$$\hat{R}(m', n') = R(m, n) \otimes \psi(m, n) \quad (11)$$

where $R(m, n)$ is the RBC image after segmentation, $\hat{R}(m', n')$ is the Gabor-wavelet-filtered RBC image, and \otimes denotes convolution. The Gabor wavelet filter is widely used to extract features that differentiate between targets with similar shapes for object classification. It is also shown that texture features extracted from Gabor filter outperform these from other methods [73]. Accordingly, the Gabor filter is utilized to extract the RBC features for the classification purposes. After applying the Gabor

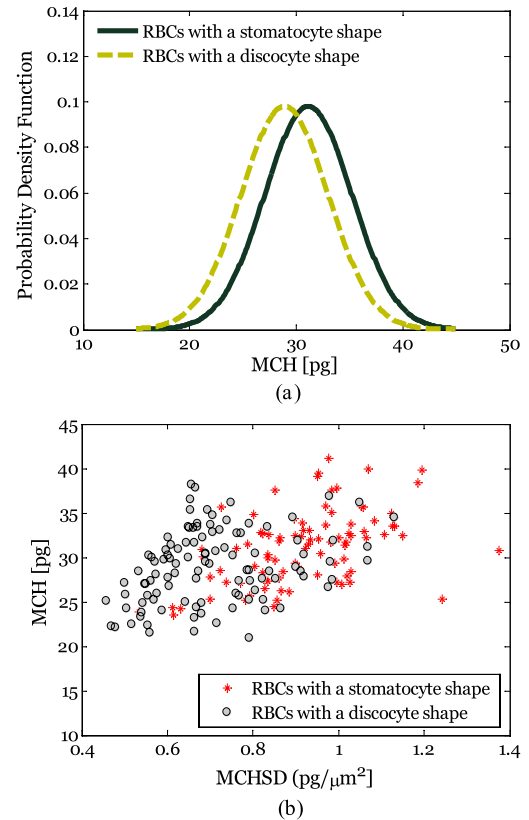


Fig. 13. (a) Statistical distributions of random variable recording the MCH based on each single RBC. (b) Scatter plot of the relationship between the MCH and MCHSD for a single RBC [41].

wavelet filter to the extracted RBCs, the features in Table 1 are measured. Features F1–F10 are identified from the whole RBC and F11–F14 are related to the inner part of the RBC on the Gabor-wavelet-filtered single RBC image.

According to Table 1, 14 features are extracted for each class of RBC. However, any dependent, redundant or irrelevant features should be excluded for the better classification results since they can degrade or confuse the classification model. Therefore, the stepwise selection of variables, a combination of the forward and backward selection methods [75] and commonly referred to as stepwise discriminant analysis, is utilized to analyze the extracted features. For the forward selection procedure, the Wilks Λ or F test is utilized to test the null hypothesis that a particular variable does not contribute to classifying the groups beyond what other existing variables yield. In this procedure, first, the Wilks $\Lambda(y_i)$ value for each individual variable is computed, where $i = 1, 2, \dots, p$ and p is the number of variables [75]. Then, the minimum $\Lambda(y_i)$ value or the maximum associated F value is chosen. For example, if y_1 is chosen in the first step, then $\Lambda(y_i|y_1)$ for each of the other $p - 1$ variables is computed and that with the minimum $\Lambda(y_i|y_1)$ or the maximum associated partial F is selected. Then we assume that y_2 is selected

Table 1 Feature Descriptions [49]

Feature	Description
Segmented Single RBC	
F1: Projected area	Number of pixels within single RBC \times one-pixel area
F2: Perimeter	Length of the cell boundary
F3: Circularity	(Perimeter \times perimeter)/area
F4: Average phase value	Average phase value for pixels within a single RBC
F5: Mean corpuscular hemoglobin (MCH)	Mean corpuscular haemoglobin
F6: MCHSD	MCH surface density
F7: Phase of moment centroid pixel	Phase value of moment centroid pixel (average 5×5 pixels)
F8: Sphericity coefficient	Phase of moment centroid pixel/maximal phase value
F9: Elongation	Orientation of Freeman chain code [49][74] in the cell boundary
F10: D value	Phase of moment centroid pixel minus maximal pixel phase value
Inner part of the segmented RBC	
F11: Projected area	Number of pixels within the inner part of RBC \times one-pixel area
F12: Perimeter	Length of the boundary in the inner part of cell
F13: Average phase value	Average phase value for pixels within the inner part of RBC
F14: Elongation	Orientation of Freeman chain code in the boundary of the inner part of cell

in the second step. This procedure continues until no more variables can be chosen. Thus, $\Lambda(y_i|y_1)$, $\Lambda(y_i|y_1, y_2), \dots, \Lambda(y_i|y_1, y_2, \dots, y_{p-1})$ are computed using [73]

$$\Lambda(x|y_1, \dots, y_p) = \frac{\Lambda(y_1, \dots, y_p, x)}{\Lambda(y_1, \dots, y_p)} \quad (12)$$

which is distributed as $\Lambda_{1, v_H, v_E - p}$ with the degrees of freedom of $v_H = k - 1$ and $v_E = k(n - 1)$, where k is the number of groups and n is the number of samples. Regarding (12), if adding the additional variable x makes $\Lambda(y_1, \dots, y_p, x)$ smaller than $\Lambda(y_1, \dots, y_p)$, then $\Lambda(x|y_1, \dots, y_p)$ is small enough such that the null hypothesis that the variable x is not useful in classifying the groups beyond which other variables would yield is rejected. Moreover, (12) can be described as follows [74]:

$$\Lambda = |E|/|E + H| \quad (13)$$

where

$$E = \sum_{i=1}^k \sum_{j=1}^n (y_{ij} - \bar{y}_i)(y_{ij} - \bar{y}_i)^T \quad (14)$$

$$H = n \sum_{i=1}^k (\bar{y}_i - \bar{y})(\bar{y}_i - \bar{y})^T$$

where y_{ij} is the j th data point of the i th group, \bar{y}_i is the mean vector of the i th group, and \bar{y} is the mean of all the sample data. The Λ statistics of (12) can also be changed into the following partial F statistic [75]:

$$F = \frac{1 - \Lambda^{v_E - p}}{\Lambda^{v_H}} \quad (15)$$

which is distributed as $F_{v_H, v_E - p}$, where $v_H = k - 1$ and $v_E = k(n - 1)$. If Λ in (12) or F in (15) is smaller than the critical values $\Lambda_{\alpha, 1, v_H, v_E - p}$ or $F_{\alpha, v_H, v_E - p}$, the null hypothesis is rejected (α is the significance level).

Similar to the forward selection operation, the backward selection begins with all the features. Then, the feature that contributes the least is excluded from the set. Two classifiers have been implemented and choosing the classifier depends on the test of equality between covariance matrices. If covariance matrices are not equal then a nonlinear classifier will be considered. Otherwise, a linear-classifier will be chosen. Eventually, the basic scheme for the RBCs classification method based on cell morphology is presented in Fig. 14.

Here 117 samples for stomatocyte RBC, 105 samples for discocyte RBCs and 100 samples for echinocyte RBCs are extracted. The training and test sets are examined and classified by an expert biologist before any further experiments. It is worth mentioning that stomatocyte and discocyte RBCs have a central part in contrast to echinocyte RBCs. The Gabor wavelet filter was applied to each RBC before the features extraction. Fig. 15 shows some of the Gabor coefficients obtained by varying the Gabor kernel frequency from 0.1 to 0.4 at intervals of 0.1 and changing the rotation angle of the Gabor kernel from 0° to 180° at 30° gaps for each kernel frequency [49].

At the next step, F1–F10 and F11–F14 were measured, the former at the entire RBC and the latter from the inner part of the RBC on the Gabor-wavelet-filtered RBC image. Four random values are generated from a standard normal distribution to be assigned to F11–F14 in which case the inner part of RBC was not detected. The importance of each feature was analyzed by applying the stepwise selection method described previously. Therefore, those features not helpful in distinguishing the three RBC groups have been excluded from the feature set. Other features will be kept untouched. Eventually, the null hypothesis revealed that ten features of F1, F2, F4,

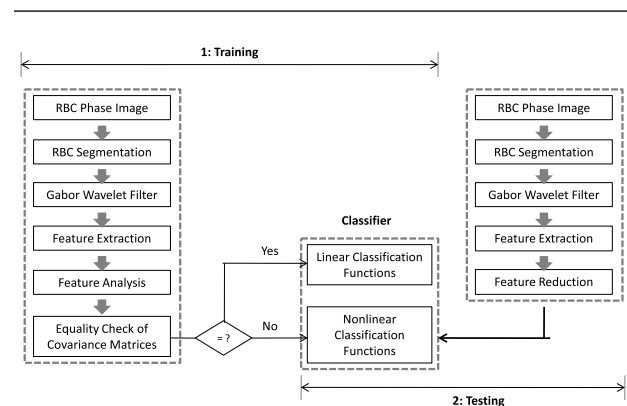


Fig. 14. Basic scheme for cell morphology-based classification of red blood cells [49].

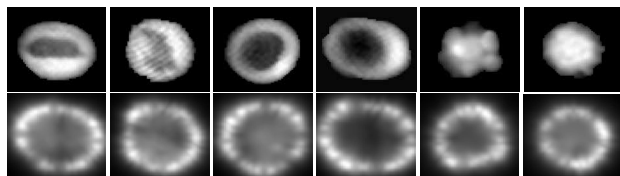


Fig. 15. Gabor-wavelet-filtered RBC images. Top row: extracted RBCs with the marker-controlled watershed transform algorithm. Bottom row: corresponding Gabor-wavelet-filtered RBCs [49].

F5, F7, F9, and F11–F14 were not redundant and were kept for designing the RBC classifier. The null hypothesis for this test was that the variable was redundant for separating the RBC groups.

The ten useful features after the stepwise selection step were used to establish the RBC classifier. The χ^2 test for the equality of the covariance matrices using the ten features was conducted with the null hypothesis that the covariance matrices for the three kinds of RBCs are the same, where $\chi^2 = 4035$ and the critical value was 162 at significance level $\alpha = 0.05$. The equivalent p -value for the null hypothesis was approximately 0 at $\alpha = 0.05$ (the null hypothesis can be rejected). This led to the adoption of the following three nonlinear discriminant functions which correspond to the three types of RBC [49]:

$$\begin{aligned}
 \text{Stomatocyte RBC : } & L_1(Y) = (y - \bar{y}_1)^T S_1^{-1} (y - \bar{y}_1) \\
 \text{Discocyte RBC : } & L_2(Y) = (y - \bar{y}_2)^T S_2^{-1} (y - \bar{y}_2) \\
 \text{Echinocyte RBC : } & L_3(Y) = (y - \bar{y}_3)^T S_3^{-1} (y - \bar{y}_3) \quad (16)
 \end{aligned}$$

where S_1 , S_2 , and S_3 are the covariance matrices and, \bar{y}_1 , \bar{y}_2 and \bar{y}_3 are the mean vectors of the three types of RBC, and y is feature vector of the unknown input RBC. Finally, a cross-validation [75] is performed to estimate the error rates of the presented RBC classification method based on individual RBC level.

Fig. 16 shows a scatter plot of the selected features. According to Fig. 16(a) and (d), we can see that there is a positive correlation between two corresponding features. Table 2 presents the classification result and the rate of misclassification for the three types of RBC based on testing set. These experimental results show that the misclassification rates of our RBC classification scheme are 0 except discocyte ones. Moreover, all the samples in training RBC set are correctly classified and the misclassification rates are 0 for the three types of RBC.

Overfitting problems are generated if we train a machine learning algorithm with dataset and use the same dataset for predictions to evaluate the proposed algorithm because the algorithm would remember every training sample during the training process and make a good prediction on the

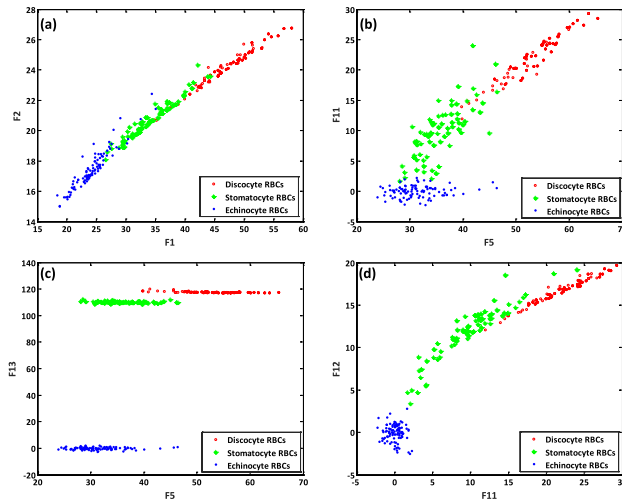


Fig. 16. Scatterplots between selected pairs of features (see Table 1) for the three types of RBCs: (a) scatterplot between features F1 and F2; (b) scatterplot between features F5 and F11; (c) scatterplot between features F5 and F13; and (d) scatterplot between features F11 and F12 [49].

training dataset. On the other hand, the algorithm may produce poor predictions on a nontraining dataset. Therefore, the best way to evaluate the performance of a classification algorithm is to make predictions for new data for which we already know the correct answers. In other words, the training and testing set should not be overlapped. Some popular techniques used to estimate the performance of classification algorithm consist of k-fold cross validation, repeated random test-train splits, and leave-one-out cross validation [76]. We have adopted the leave-one-out cross validation method to evaluate the RBC classification algorithm because more observation data (that is, the total observation data minus one) can be used as a training set and all observations can be used as a testing set that would be circularly predicted in this approach. For the experiments presented, the misclassification rates of our proposed classification algorithm for the three types of RBC (stomatocyte, discocyte, and echinocyte RBC) are 0, 0.95%, and 0, respectively. Moreover, the area under receiver operating characteristic (ROC) curve [76] which is another important classification metrics is used to evaluate our classification algorithm. The average area under the curve (AUC) [76] for the proposed

Table 2 Results of the Classification of the Three Types of RBCs Using the Presented Classifier [49]

Actual group	Sample number	Predicted group			Mis-Classification rate (%)
		Stomatocyte	Discocyte	Echinocyte	
Stomatocyte	117	117	0	0	0
Discocyte	105	1	104	0	0.95
Echinocyte	100	0	0	100	0

RBC classification scheme was measured to be 0.9984. The low misclassification rates and high average area under the curve reveal the robustness of our proposed classification algorithm. In the experiments, our method focuses on the classification of three main types of RBCs while there are various types of RBCs. Therefore, our system may produce a wrong prediction for an RBC that does not belong to one of these three types. However, the system can be improved by developing a classification algorithm by introducing more types of RBC in the training dataset in the future.

D. Label Free Identification of Healthy and Malaria Infected Red Blood Cells

Malaria is one of the potentially life threatening blood related diseases found especially in Africa and Asia. Medication and cure of malaria requires its correct and early diagnosis. Malaria is diagnosed by identifying the parasite itself in the red blood cells or by identifying the response of the blood cells to its presence. Samples are stained with chemicals which get attached to malaria parasites, changing the absorption profile of the cell. Investigation of stained blood smears under a bright field microscope by a trained health care professional is the best method to identify malaria [77]. But especially in developing countries, due to lack of sufficiently trained technicians, good quality instruments and chemicals, visual identification of malaria infected RBCs becomes difficult and unreliable. Also, study of how the parasite affects and changes the red blood cells and its physiology will be useful in early malaria diagnosis and to design drugs for its treatment. Quantitative phase microscopy, including digital holographic microscopy, can provide a multitude of blood cell parameters based on the quantitative phase images [31], [51], [53], which could be used to study the effect of the malaria parasite on the red blood cells as well as to discriminate healthy and malaria infected samples without the need of any labeling agents [40], [48]. In this section the use of DH-QPM in cell parameter extraction, study of cell physiology and cell identification for blood samples affected by malaria is overviewed.

Thin blood smears of centrifuged healthy and severe malaria blood samples were made on a microscope slide for observation under the digital holographic microscope. The microscope employed a $100\times$ oil immersion microscope objective lens with $NA = 1.25$ used in dry mode along with a He-Ne laser working at 611 nm and an 8-bit CCD array with $4.65\text{-}\mu\text{m}$ pixel pitch. Reconstructed quantitative phase distributions for representative cells from healthy and malaria infected samples are shown in Fig. 17.

A total of 52 cells from a healthy sample and 45 cells from malaria tested positive (Giemsa test) were used in the study. The locations of the cells were determined automatically by thresholding the obtained phase distributions by the

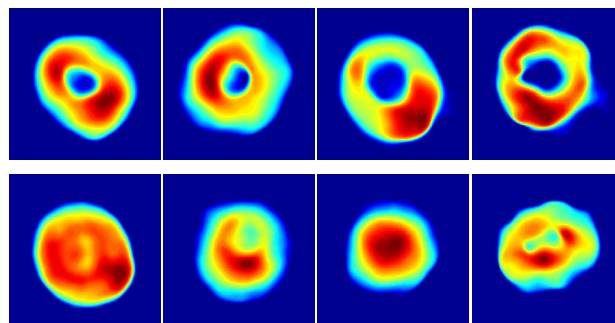


Fig. 17. Quantitative phase profiles at the image plane for, healthy cells (top row) and malaria infected cells (bottom row) [38].

background phase distribution [38]. From the phase maps it can be seen that the predominantly biconcave disk shape in the case of healthy cells has changed to a much more spherical shape in the case of the malarial sample.

Many important cell parameters can be extracted from the phase profile of the cells. OPL represents the product of the cell's index of refraction and thickness is computed from the phase profile using (5). The mean OPL is a measure of many cell parameters including cell dry mass and hemoglobin content. It can be written as

$$OPL_{\text{mean}} = \frac{1}{N} \sum_{i=1}^N OPL_i \quad (17)$$

OPL_i is the OPL at i th pixel of the optical thickness map and N is the total number of pixels occupied by the cell on a flat surface. Optical volume represents the effect of the contents of the cell and the thickness of the cell on the light beam passing through it. It is proportional to the optical thickness through

$$V_{\text{optical}} = dA \sum_{i=1}^N OPL_i \quad (18)$$

where dA is the area each pixel represents at the image plane and is given by $dA = \Delta x^2 / M^2$ (Δx is the camera pixel size and M is the lateral magnification of the system). One of the important parameters in the case of red blood cells is the surface area to volume ratio. The biconcave disk shape of the red blood cells is of particular importance as it increases this ratio, thereby increasing the chances of oxygen permeating the membrane of the cell. The optical surface area (OSA) is given by [78]

$$OSA = dA \sum_{i=1}^X \sum_{k=1}^Y \sqrt{1 + \delta h_x^2(i, k) + \delta h_y^2(i, k)} + PA \quad (19)$$

δh_x and δh_y are the gradients along the x and y directions of the cell thickness profile and i and k is the position of the pixel in the region where the cell existed. Other parameters that can be extracted using the OPL profile include: coefficient of variation of the optical thickness indicating the thickness distribution around the mean

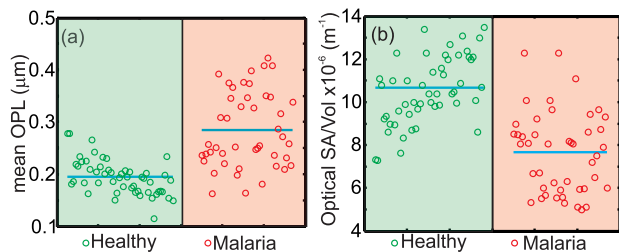


Fig. 18. Measured cell parameters based on its spatially varying OPL profile (shape) of the cell. (a) Mean OPL. (b) OSA-to-volume ratio. Mean values of the parameters are shown as continuous lines.

value and the flatness of the cell, diameter of the cell, sphericity index of the cell indicating its roundness, and statistical parameters of OPL distribution such as its skewness and kurtosis which together provide the flatness and symmetry of the cell [78]. Table 3 gives the values of the parameters for healthy and malaria samples. Not all these parameters provide an insight into the state of health of the cell. Fig. 18 shows the scatter plot of measured mean OPL and optical surface to volume ratio. These parameters are of importance because they provide information about the shape and flatness of the cells.

The mean of the OPL distribution for cells infected by the malaria parasite is higher. This is expected since the presence of the parasite increases the OPL of light propagating through the cells. The surface to volume ratio is less in the case of a malaria sample. Together these two parameters indicate that the malaria infected cells have different spatially varying optical paths (shape) compared to healthy cells. So the shape of the cell may be used to discriminate between the cells. The Pearson product-moment correlation coefficient between shapes of healthy and malaria infected red blood cells were used for this [40]. The thickness distribution obtained at different axial depths of the object by numerical focusing

Table 3 Red Blood Cells—Physical Parameters

Parameter	Healthy sample	Malaria positive sample
Maximum OPL* (μm)	0.29±0.044	0.29±0.087
Mean OPL* (μm)	0.19±0.032	0.28±0.073
Coefficient of variation (CV) (CV) of OPL*	0.29±0.038	0.20±0.065
Optical volume (fL)	17.89±3.41	21.75±9.84
Projected area × 10 ¹² (m ²)	46.04±6.48	43.87±17.07
Diameter (μm)	7.62±0.54	7.31±1.37
Optical Surface Area by volume ratio × 10 ⁻⁶ (m ⁻¹)	10.67±1.82	7.67±1.91
Sphericity index	0.178±0.023	0.243±0.051
Skewness of thickness distribution	-0.158±0.022	-0.155±0.09
Kurtosis of thickness distribution	1.969±0.178	2.195±0.470

* OPL: Optical path length

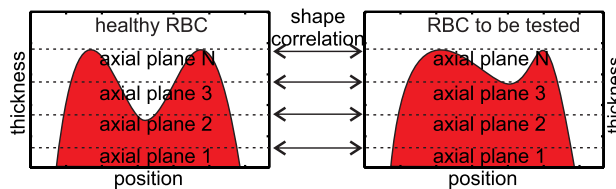


Fig. 19. Cell identification by shape comparison.

(Fig. 19) was used to compute the shape correlation coefficient. Fig. 20 shows the probability distribution of the measured correlation values along with the scatter plot of the values for individual cells.

Mean values of shape correlation coefficients for healthy and malaria infected cells are shown by solid blue lines. Average of these means (solid black line) acted as the discrimination threshold. Using this threshold the true positive rate of identification comes out to be better than 95% and the false positive rate is about 3%.

A digital holographic microscope has the potential to study the bio-physical properties of the cell using the shape-based parameters. These parameters can be used to visualize the physiology of the cells and can also be used as a base for cell discrimination.

E. Automated Quantitative Analysis of Cardiomyocytes

Cardiomyocytes cells or myocytes are the main contractile elements of the heart muscle. These cells work entirely to generate human heart beating and control blood flow through the blood vessels and capillaries of the circulatory system. Cardiomyocytes make up the atria, and the ventricles; the former are the chambers in which blood enters the heart and the latter are the chambers where blood is collected and pumped out of the heart. These cells must be able to shorten and lengthen their fibers and the fibers must

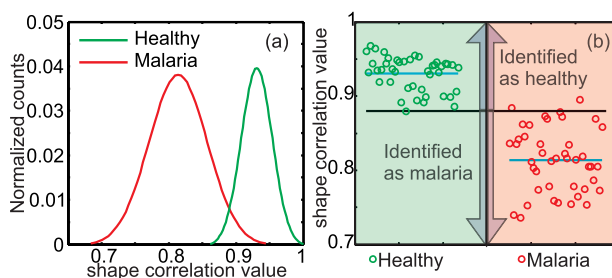


Fig. 20. Label free identification of malaria infected red blood cells. (a) Probability distribution of shape correlation values. (b) Computed correlation coefficient between different cell combinations. The average of shape correlation coefficient for healthy-healthy (O) and healthy-malaria (O) combinations (straight black line) acts discrimination parameter.

be flexible enough to stretch. These functions are critical to the proper form during the beating of the heart [37].

During the lengthy drug discovery process, it is crucial to detect toxic compounds early, through safety profiling assays in the process before significant time and important financial investments are made. Therefore, researchers and companies in the fields of medicine have to ensure that the effect of lead candidate compounds on cardiac function strictly satisfy safety criteria. Consequently, it is important to establish more informative in vitro cardiotoxicity screens and data analysis algorithms at the early stages of drug development for preventing late stage failure [79], [80].

We will show that by taking advantage of the DH-QPM technique integrated with information processing algorithms it is possible to measure dynamic properties of beating cardiomyocytes in an automated manner. Experimental results revealed that beating parameters of cardiomyocytes can be obtained by the automated algorithm based on digital holographic quantitative phase microscopy phase signal analysis. Our method is fast, contactless and effective enough to allow for automated analysis between normal cardiomyocyte dynamics and all other abnormal activities. The proposed procedure can enable screening cardio-toxicological or profiling of candidate molecules in preclinical drug discovery and safety testing programs.

The 3-D reconstruction process can be achieved at a speed of 100 images per second depending on the PC computer power. The QPIs are based on OPD defined as follows [47]:

$$\text{OPD}(x,y) = d(x,y) \times [n_c(x,y) - n_m] \quad (20)$$

where $d(x, y)$ is the cell's thickness, $n_c(x, y)$ is the average intracellular refractive index integrated along the optical axis at the (x, y) position and n_m is the constant refractive index of the surrounding medium. The OPD is similar to OPL as defined in (5). For the quantitative analysis of cardiomyocyte dynamics, we calculated the beating activity using two alternative methods, average and variance of OPD images. The contraction and relaxation feature of cardiomyocyte were also measured using the proposed automated procedure.

F. Cardiomyocytes Beating Profile Measurement Using Averaged OPD Images

The beating profile of cardiomyocytes was computed from thresholding the cardiomyocyte OPD images with a threshold value of 10% of the maximum OPD signal and then the thresholded images were averaged. The threshold value is utilized to suppress the effect of noise. We realized that beating profile under different threshold does not affect final beating profile significantly

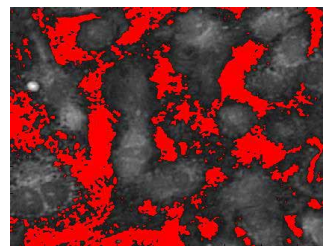


Fig. 21. An example of the thresholded cardiomyocyte image (red color denotes background after thresholding).

(data not shown). An example of the thresholded cardiomyocyte images is presented in Fig. 21. The beating profile, after applying (20), is shown in Fig. 22 (inset is the magnified part on the beating pattern). Then, multiple parameters based on beating profile in Fig. 23 were derived. These parameters are described in Table 4.

To measure the desired characteristics properties of beating profile, peaks shall be detected. It is possible by applying the first derivative technique to the beating curve (Fig. 22) and finding locations where the first derivative values are zeros. It should be noted that the beating periods calculated between two negative peaks are approximately equal to that between two positive peaks. Consequently, the beating profile between two adjacent negative peaks considered as one beating period should be also extracted (see Fig. 23). There are some other beating properties which

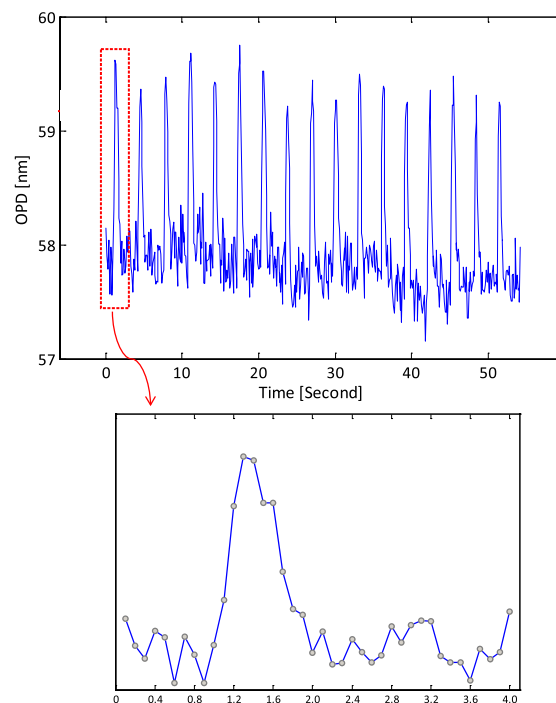


Fig. 22. Beating profile of cardiomyocyte (inset shows a single beat) [47].

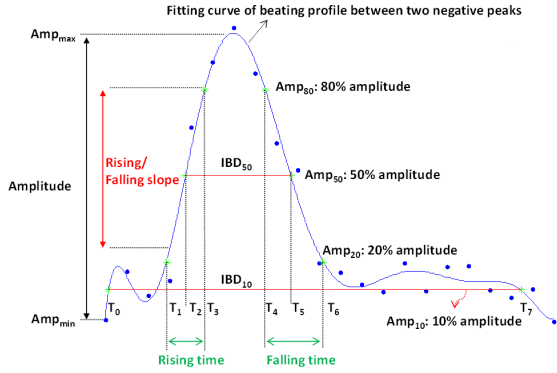


Fig. 23. Explanation of the fitted curves with parameters during one beating period on cardiomyocytes beating activity [47].

should be calculated from the fitted curve on the raw beating profile. Therefore, the extracted beating profile for each beating period is fitted with 9th-degree polynomials in the least square criterion. One of the fitting polynomial curves and the parameters are given in Fig. 23.

Regarding the fitted polynomials curves, the amplitude value defined in Table 4 can be calculated as the maximum value minus the minimum value on the fitted curve. Thus, the corresponding time (unit is second) in x -axis for Amp10, Amp20, Amp50, Amp80 (see Fig. 23) can be also calculated by solving the fitted polynomial equation. Then, all of the mentioned parameters for each individual beating period can be calculated.

G. Cardiomyocytes Beating Profile Measurement Using Variance of OPD

We also propose an alternative way, less sensitive to noise, to calculate the beating profile of cardiomyocytes to measure the variance of each OPD image after the temporal mean of the image stack is subtracted. This method is illustrated by (15) [47]

$$\delta_{\text{opd}}^{(i)} = \text{variance}[\text{opd}(x,y)^{(i)} - \overline{\text{opd}}_{\text{temp}}] \quad (21)$$

where $\text{opd}(x,y)^{(i)}$ is the i th OPD image ($1 \leq x \leq M$ and $1 \leq y \leq N$, M and N are the sizes of cardiomyocyte OPD image), $\delta_{\text{opd}}^{(i)}$ represents the variance of the i th cardiomyocyte image after temporal mean subtracted and $\overline{\text{opd}}_{\text{temp}}$ is the temporal mean which is calculated as the mean value of the stacked images in the temporal dimension.

The peaks are detected by applying the first derivation method. In addition, the positive and negative peaks are screened with a threshold value obtained by Otsu's method. Consequently, the minimum negative peak between two neighboring positive peaks and the maximum positive peak between two neighboring negative peaks are selected. Similar to the previous section the beating profile within one beating period can be individually extracted and is

Table 4 Characteristic Parameters of Cardiomyocyte [47]

Parameter	Definition
Amplitude	Value difference from each positive peak to the following negative peak (Amplitude = $\text{Amp}_{\text{max}} - \text{Amp}_{\text{min}}$) [see Fig. 23]
Rising time	The time elapsed from Amp_{20} to Amp_{80} ($=T_3 - T_1$) [see Fig. 23]
Falling time	The time elapsed from Amp_{80} to Amp_{20} ($=T_6 - T_4$) [see Fig. 23]
IBD_{50}	The time elapsed for two points compose one Amp_{50} ($=T_5 - T_2$) [see Fig. 23]
IBD_{10}	The time elapsed for two points compose on Amp_{10} ($=T_7 - T_0$) [see Fig. 23]
Rising/ Falling slope	The change of increased/decreased amplitude over the time course between Amp_{80} and Amp_{20} ($=\text{Amp}_{80} - \text{Amp}_{20}$) [see Fig. 23]
Beating rate	The total number of positive/negative peaks in 1 minute ($=$ total number of positive peaks/total time)
Beating period	The time between two adjacent positive and/or negative peaks ($=$ the time of i_{th} positive peak $-$ the time of $(i-1)_{\text{th}}$ positive peak)
Frequency	The number of beating period per second ($=$ total number of beating period/total time)

fitted with the polynomial equation of degree 9 in a least square error sense. Finally, the same parameters similar to the previous method are calculated and were found to be in excellent agreement with the reported results [79].

H. Cardiomyocytes Contraction and Relaxation Measurement

The contraction and relaxation feature of cardiomyocyte can be obtained as follows. 1) Each captured image in the temporal stack is subtracted from the following one. 2) The spatial variance of the OPD is measured. 3) Quantify the amount of spatial displacement between successive frames. The output contains cardiomyocytes contraction and relaxation information [Fig. 24(a)]. According to Fig. 24, one higher peak is for contraction and the neighboring lower peak is for the relaxation. The peaks can be detected with the first derivative criterion. Similarly, positive peaks for contraction can be properly extracted with Otsu's thresholding algorithm by using all of the detected positive peaks. Next, a maximum peak between two neighboring contraction peaks is chosen as a positive peak for relaxation. The resulting curves from Fig. 24(a) with the selected peaks are shown in Fig. 24(b).

Finally, the detected peaks can be utilized to measure the beating rate, beating period and frequency for cardiomyocytes contraction and relaxation. In addition, the interval for cardiomyocytes contraction and the relaxation can also be calculated with the detected peaks in Fig. 24(b). It is noted that the proposed methods can result in similar outputs concerning beating rate, beating period and frequency by using the same cardiomyocyte image pools.

The results and data presented in Section V illustrate that two-beam digital holographic quantitative phase

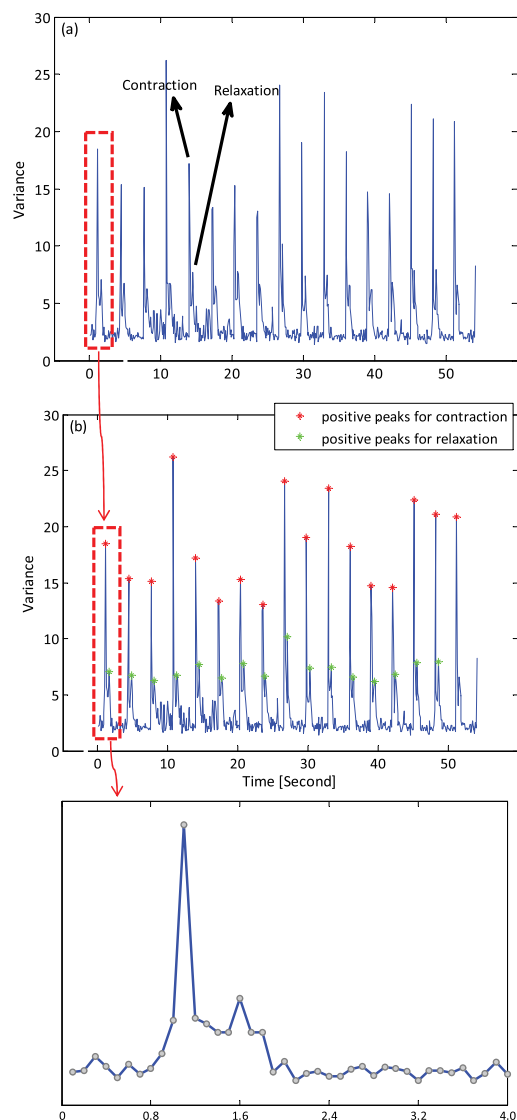


Fig. 24. Cardiomyocytes beating profile with contraction and relaxation information. (a) Original data of cardiomyocytes beating profile. (b) Cardiomyocytes beating profile with selected peaks for the contraction and relaxation measurements (inset shows a single beat with contraction and relaxation peaks) [47].

microscopy can be an effective tool to study the biophysical properties of cells and tissues. The extracted parameters provide insight into the working of the cell.

VI. SELF-REFERENCING DIGITAL HOLOGRAPHIC MICROSCOPY

The two-beam digital holographic microscope employing Mach-Zehnder geometry, discussed in the previous section, is capable of providing accurate and detailed QPIs of cells. But as can be seen from Fig. 6, implementation of this microscope requires optical

elements for beam-splitting and beam combining. So a compact, portable version of the microscope is difficult to realize. Also the ratio of the object and reference beams needs to be adjusted properly for high contrast interference fringes. In Mach-Zehnder geometry, as the two beams travel along different paths, they may pick up uncorrelated path length changes leading to lower temporal phase stability, without a vibration isolation system. In common path geometry, in which the reference beam is usually derived from the object beam itself, the two beams travel along the same path and encounter the same set of optical elements. This reduces the effect of uncorrelated path lengths increasing the temporal stability of the system [50]–[54]. High temporal stability is a must to study fluctuations in cell thickness profile. One way to implement common path geometry is to convert a portion of the object wavefront into a separate reference beam by spatial filtering [50]–[54]. This requires optics for Fourier transformation of the object beam as well as its spatial filtering. An easier and simpler way to achieve common path geometry is by the use of self-referencing geometry [55]–[60]. In SRDHM, a portion of the object wavefront, which is not modulated by the object information act as the reference and is made to interfere with the portions of the same wavefront, which is modulated by the object [55]–[60]. This makes the implementation of the setup easy, paving the way for compact, portable and highly temporally stable (without vibration isolation) digital holographic microscopes. In this section we review our work on SRDHM and its application for imaging of cell dynamics with subnanometer temporal stability and its use in studying bio-physical aspects of cells and their identification [56]–[59].

A. Lateral Shearing SRDHM

One of the simplest ways to implement self-referencing geometry is to use a beam-splitting element to create two copies of the object wavefront and make them interfere at the sensor plane [55], [56], [58]–[60]. This can be achieved using Michelson interferometer geometry [55], [60], where the object beams reflected from two mirrors interfere to create the holograms. Use of two mirrors add to the complexity of the setup and reduce its temporal stability. Another implementation used a mirror to fold a part of the object beam back on to itself by the use of a mirror [57]. Here also the use of a separate mirror impedes the time stability of the system. The easiest way to implement self-referencing geometry is to use a lateral shearing geometry as shown in Fig. 25 [56], [58]. A light beam derived from a laser diode module ($\lambda = 635$ nm) is used to transilluminate the cells. This is then magnified by a microscope objective lens. Reflection from the front and back surface of a thick glass plate (thickness ~ 4 mm)

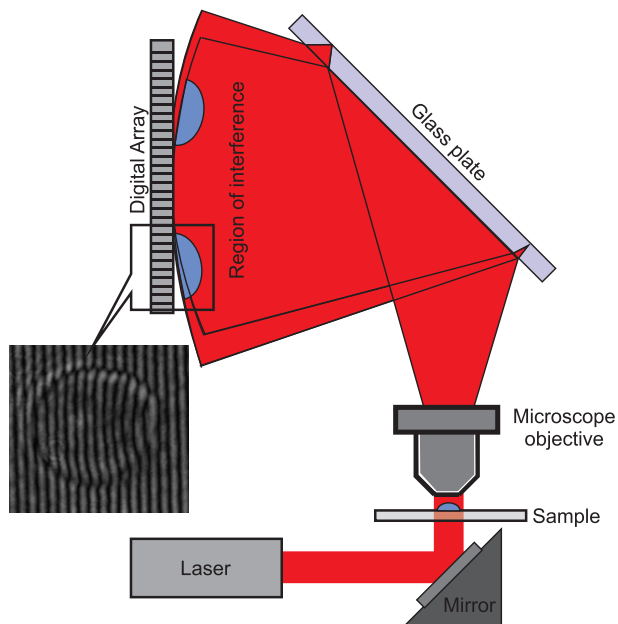


Fig. 25. Self-referencing digital holographic microscope based on lateral shearing configuration [56].

made up of fused silica (refractive index = 1.457 at 635 nm) creates two versions of the object wavefront. They will be laterally displaced with each other when they reach the sensor plane where they interfere to form the holograms [82]. The amount of the lateral shift between the objects at the sensor plane depends upon the refractive index of the glass plate, thickness of the glass plate and angle of incidence of the wavefront at the glass plate. For sensor sizes ($\sim 5 \text{ mm} \times 5 \text{ mm}$) much less than the size of the magnified wavefront, it can be assumed that all portions of the wavefront are incident on the shearing glass plate at the same angle. The lateral shift between the wavefronts can then be calculated to be approximately 3 mm [82].

If the lateral shear is much greater than the size of the magnified object at the hologram plane, then the image of the object from the front and back surface of the glass plate will not overlap, making it possible for portions of one of the wavefronts without object modulation to overlap with regions of its copy containing object information, creating holograms rather than shearograms [56], [58]. This leads to lateral shearing digital holographic microscope (LSDHM). Holograms of glass $10\text{-}\mu\text{m}$ diameter microspheres recorded in the case of LSDHM using a microscope objective lens of $40\times$ magnification and $\text{NA} = 0.65$ using an 8-bit CCD array of $4.65\text{-}\mu\text{m}$ pixel pitch is shown in Fig. 26(a). Interference fringes formed by the object wavefronts from the front and back surface of the glass plate have opposite curvatures [Fig. 26(b) and (c)]. This can be understood from Fig. 25, which shows

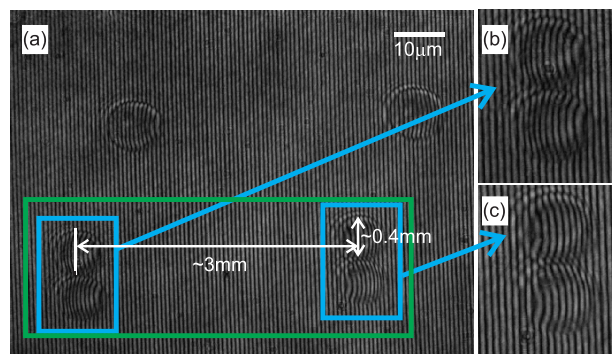


Fig. 26. Hologram recorded by LSDHM. (a) Whole field of view. (b), (c) Hologram formed by object wave reflected from the front and back surface of the glass plate, respectively.

that the reference wavefront lags the object wavefront reflected from the front surface, and it leads object wavefront reflected from the back surface. From Fig. 26(a) it can be seen that the shear amount is greater than the size of the magnified object.

Interference pattern shown in Fig. 26 can be regarded as a hologram and hence reconstructed just like a normal digital hologram. In this case also an object hologram with the object present in the field of view and a reference hologram with the medium surrounding the object in the field of view were recorded for extraction of quantitative phase information. Fig. 27 shows the reconstruct phase profile [inside the green rectangle in Fig. 26(a)] of $10\text{-}\mu\text{m}$ polystyrene microspheres of refractive index 1.58, immersed in oil of refractive index 1.53 obtained after numerical reconstruction of the hologram shown in Fig. 26(a).

Thickness distribution of the microspheres shown in Fig. 27(b) was computed using (5) after substituting for the refractive index values. Cross-sectional thickness profile [Fig. 27(c)] shows the ability of the technique for accurate thickness reconstructions.

B. Temporal Stability of LSDHM

LSDHM uses only a few optical elements and the object and reference beams travel along the same path while encountering the same set of optical elements. This will greatly improve the temporal stability of the setup making it possible to measure thickness fluctuations of cells under various conditions. Temporal stability of the technique was measured by recording a time series of holograms while keeping a blank microscope slide in the sample holder. In the present case holograms were recorded at the rate of 30 Hz for 10 s (total of 300 holograms). These holograms were numerically reconstructed to extract the time varying phase profiles and the mean of the phase fluctuations at 10000 randomly selected points from the entire field of view which acts as

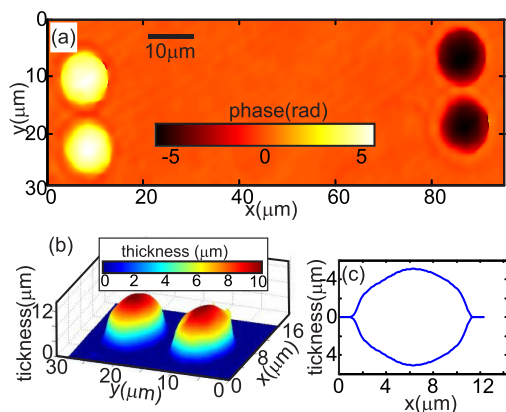


Fig. 27. Experimental results with LSDHM. (a) Quantitative phase profile inside the green rectangle shown in Fig. 26(a) obtained after phase subtraction. (b) Computed thickness distribution. (c) Cross sectional thickness variation.

the temporal stability of the device. Fig. 28(a) gives a representative plot, which shows the time varying phase profile at one of these randomly selected points. Fig. 28(b) is the histogram of the phase fluctuation for all the considered points [56]. The mean value of all these fluctuations corresponds to an optical thickness variation of 0.66 nm for duration of 10 s. These experiments were conducted on a normal wooden table without any vibration isolation mechanism. Sub-nanometer temporal stability has been observed over longer duration also [56]. Along with its compactness, the temporal stability of the device makes it an attractive tool for extraction of both physical and mechanical parameters of cells under study.

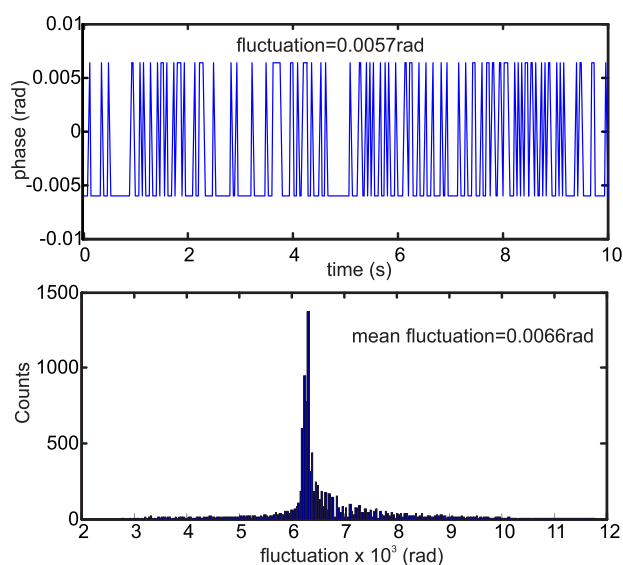


Fig. 28. Temporal stability of LSDHM. (a) Phase variation at a single spatial point. (b) Histogram of the fluctuations from 10000 random spatial points.

C. Biophysical Studies of Human Red Blood Cells

In the case of red blood cells the physical and mechanical properties of the cell depends upon the contents of the cell including hemoglobin. Physical parameters of the cells can be extracted from a single hologram and from a time series of holograms, its mechanical parameters can also be obtained [82]. These parameters may be useful in identifying its state of health, cell contents and shedding light on its biophysical properties.

To compute the mechanical parameters of the cells holograms were recorded at the rate of 30 Hz using an 8-bit CCD array with pixel pitch of 4.65 μm. A 20 × microscope objective with NA = 0.4 was used to magnify the cells. Fig. 29 shows the time variation in cell thickness fluctuation for a red blood cell extracted from sample with measured hemoglobin (Hb) content of 13.4g/dL.

Fluctuation profile of the cell for each second is computed from the standard deviation of phase profile reconstructed from a series of holograms recorded for a second at the rate of 30 Hz. The obtained fluctuation values matches those reported in literature [83]. From the fluctuation profile amplitude and frequency of the cell thickness fluctuations can be measured. Mechanical parameters for red blood cells from samples with different hemoglobin concentration are shown in Fig. 30.

From the physical and mechanical parameters, it was found that as the hemoglobin content in the red blood cell increases, the volume of the cell increases and the surface to volume ratio decreases. Fig. 30 also indicates that as the hemoglobin level increases there is a decrease in the amplitude of thickness fluctuation and increase in frequency of thickness fluctuations. All these are indicative of a tightening of the red blood cell membrane. The extracted cell parameters are sensitive to the cell content. So this technique can be used to quantify the cell content. This in turn can be used to identify diseases affecting the cells.

D. Toward Portable LSDHM

LSDHM provides QPIs comparable to that of the digital holographic microscope based on Mach-Zehnder

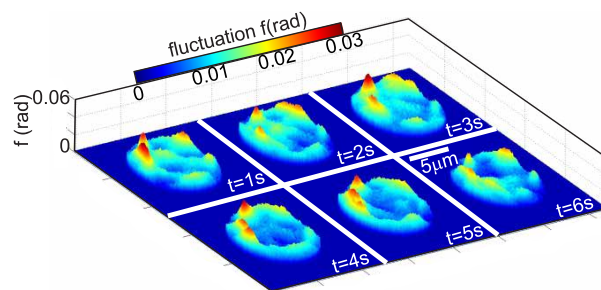


Fig. 29. Time varying thickness fluctuation in the case of human red blood cell.

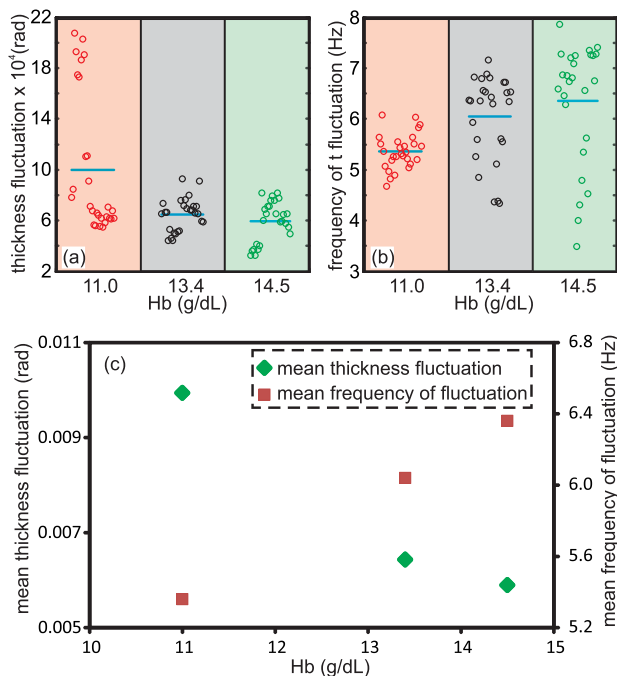


Fig. 30. Mechanical parameters of red blood cells from samples with different hemoglobin concentration. (a) Amplitude of thickness fluctuation. (b) Frequency of thickness fluctuation. (c) Variation of mean value of amplitude and frequency of thickness fluctuation with hemoglobin concentration

configuration. It has the added advantage of high temporal stability without vibration isolation, while being compact and easy to implement, requiring very few optical elements.

All these properties make it an ideal candidate for applications requiring portability. Also, now with the availability of low cost laser diode modules and cheap digital arrays like webcams, it is possible to construct a compact, portable and inexpensive quantitative phase imaging unit. Fig. 31 shows the photograph of the portable 3-D imaging module, which was 3-D printed. It used an off the shelf microscope objective lens, a laser diode module, a 5-mm-thick fused silica glass plate and a digital array.

Low cost version of the system in Fig. 31 used a VGA webcam array (3.2- μm pixel pitch). Software for hologram acquisition, reconstruction, physical and mechanical cell parameter extraction was developed in-house. Fig. 32 shows the QPIs of human red blood cells obtained with the webcam sensor using a 20 \times magnifying lens with numerical aperture (NA) of 0.4. It can be seen that even the low cost version provides detailed phase maps of the cells.

A series of holograms recorded with device also provides the thickness fluctuations of the cells under investigation as shown in Fig. 33.

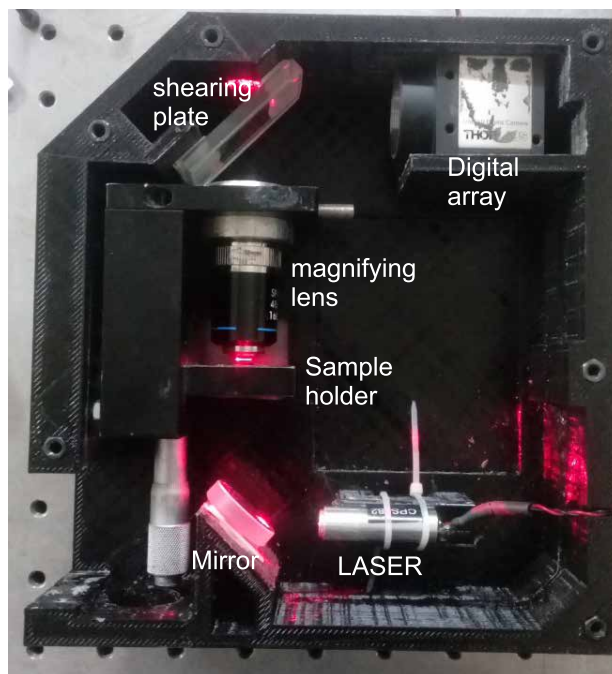


Fig. 31. Compact, portable and inexpensive LSDHM. The dimensions of the system are 19 cm x 17 cm x 6 x 6 cm (height x width x depth).

The device provides phase and fluctuation profiles of the cells in real time. This portable unit also provides many important physical and mechanical cell parameters, usually measured using hematological analyzers, without manual intervention.

Nowadays, even low-cost smartphones have mega pixel cameras, fast processors and large memory. These phones can

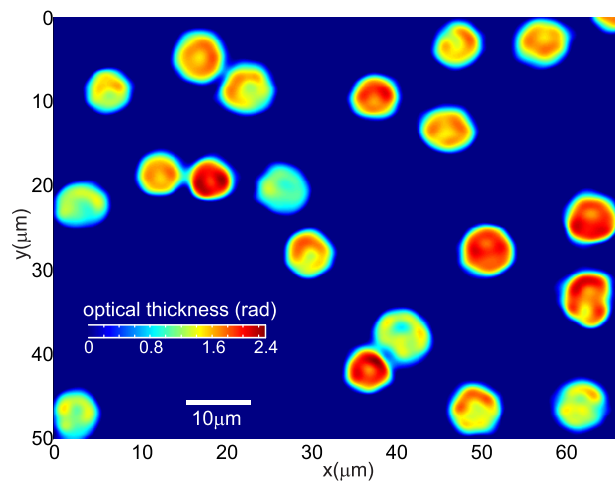


Fig. 32. Live quantitative phase profile of human red blood cells obtained with low-cost portable version of LSDHM employing a VGA webcam (see Fig. 31).

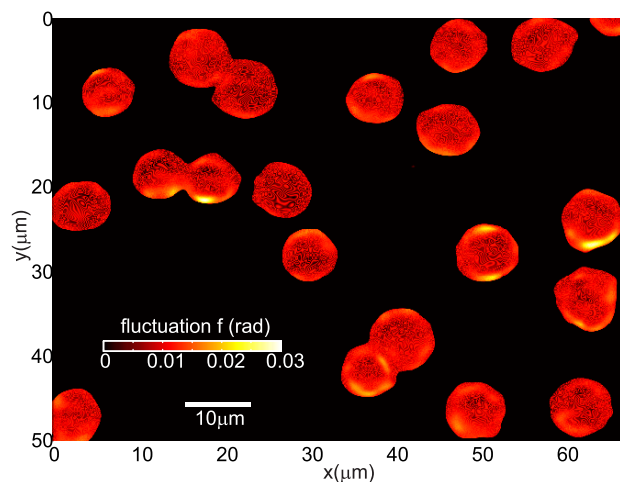


Fig. 33. Thickness fluctuation of human red blood cell shown in Fig. 32.

therefore be used to record, reconstruct and analyze holograms as well as for cell parameter extraction. Smartphones can be easily integrated into an LSDHM unit by using an eyepiece.

Fig. 34(a) shows a hologram of a 10- μm diameter polystyrene bead immersed in oil, extracted from a 1080 p video recorded by a smartphone camera with 1.4- μm pixel pitch. Numerical reconstructions [Fig. 40(c) and (d)] were carried

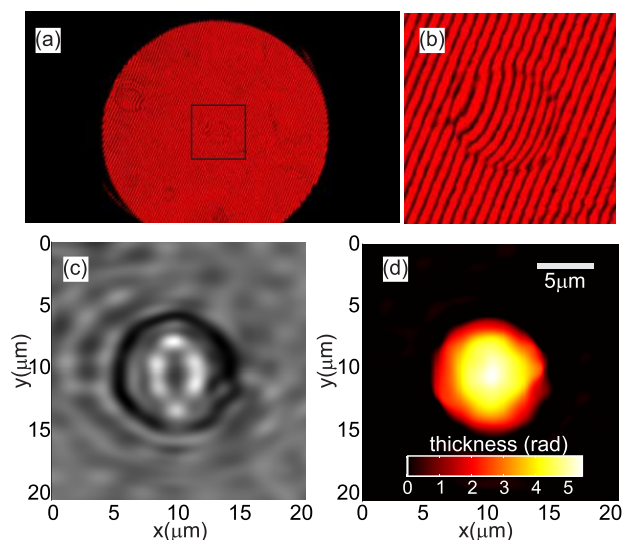


Fig. 34. Smartphone-based LSDHM. (a) Hologram extracted from a video recorded at 1080 p. (b) Region of interest inside the rectangle in Fig. 34(a). (c) Intensity reconstruction at the image plane. (d) Quantitative phase profile of the object.

out in an off-site personal computer, after transmitting the recorded holograms through Wi-Fi. The use of smartphones for recording of holograms makes the device portability higher and opens the possibility of remote diagnosis and telemedicine by using this device. Additionally, 3-D printing provides the capability for low cost large scale manufacturing of the system [86].

VII. ROAD AHEAD

Since digital holography with classification algorithms was proposed for automated cell identification and recognition [8], many variations of digital holographic microscopes have been reported for cell detection and identification, cell counting, identifying diseased red blood cells, etc. [9]–[12], [14]–[16], [34], [35], [40]–[43], [45]–[49], [84]–[90]. Digital holographic microscopes provide a real-time, label-free, high contrast quantitative phase profile of cells under various environments. The phase profile of the cell is directly related to its thickness profile and hence cell morphology can be obtained from a single hologram. This leads to extraction of physical parameters based on the cell shape. Also, from a series of holograms the mechanical properties of the cells and their dynamics can be studied and cell parameters based on time-varying morphology can be extracted. These parameters are useful in cell classification, identification and chemical free disease diagnosis, which will be a boon for clinicians. Biophysical aspects of cells, which will shed information on its physiology and growth, can also be investigated. So this tool will be helpful to researchers in studying new cells as well as those who work on designing new drugs, especially those which target specific cells. An inexpensive, compact, field portable version of the 3-D microscope using self-referencing geometry and/or lens-less systems employing pseudorandom encoding [84] may be ideal for on-field applications [85]. When coupled with a mobile device, it becomes an ideal tool for remote disease diagnosis and treatment.

Testing of the device for its potential clinical applications, initially as a hematology analyzer, is the next logical step. This requires the involvement of researchers especially from the area of life sciences. Algorithms providing better cell discrimination capability by combining both physical and mechanical parameters and cell dynamics obtained using the device will be developed. Also this device has so far been tested in the laboratory environment, which may not mimic on-field conditions. So, another direction in which work is progressing is in testing the ability of the device for cell identification in the field. ■

REFERENCES

- [1] D. B. Murphy, *Fundamentals of Light Microscopy and Electronic Imaging*. New York, NY, USA: Wiley, 2001.
- [2] F. Zernike, "Phase contrast, a new method for the microscopic observation of transparent objects," *Physica*, vol. 9, no. 7, pp. 686–698, 1942.
- [3] G. Nomarski, "Microinterferométrie différentielle et ondes polarisées," *J. Phys. Radium*, vol. 16, pp. 9–135, 1955.
- [4] P. Ferraro, A. Wax, and Z. Zalevsky, *Coherent Light Microscopy: Imaging and Quantitative Phase Analysis*. Berlin, Germany: Springer, 2011.
- [5] D. Gabor, "A new microscopic principle," *Nature*, vol. 161, pp. 777–778, May 1948.
- [6] T. Zhang and I. Yamaguchi, "Three-dimensional microscopy with phase-shifting digital holography," *Opt. Lett.*, vol. 23, no. 15, pp. 1221–1223, 1998.
- [7] L. Repetto, E. Piano, and C. Pontiggia, "Lensless digital holographic microscope with light-emitting diode illumination," *Opt. Lett.*, vol. 29, no. 10, pp. 1132–1134, 2004.
- [8] B. Javidi, I. Moon, S. Yeom, and E. Carapezza, "Three-dimensional imaging and recognition of microorganism using single-exposure on-line (SEOL) digital holography," *Opt. Exp.*, vol. 13, no. 12, pp. 4492–4506, 2005.
- [9] I. Moon and B. Javidi, "Volumetric three-dimensional recognition of biological microorganisms using multivariate statistical method and digital holography," *J. Bio. Opt.*, vol. 11, no. 6, p. 064004, 2006.
- [10] I. Moon and B. Javidi, "3D identification of stem cells by computational holographic imaging," *J. Roy. Soc. Interface*, vol. 4, no. 13, pp. 305–313, 2007.
- [11] A. Stern and B. Javidi, "Theoretical analysis of three-dimensional imaging and recognition of micro-organisms with a single-exposure on-line holographic microscope," *J. Opt. Soc. Amer. A*, vol. 24, no. 1, pp. 163–168, 2007.
- [12] I. Moon and B. Javidi, "3-D visualization and identification of biological microorganisms using partially temporal incoherent light in-line computational holographic imaging," *IEEE Trans. Med. Imag.*, vol. 27, no. 12, pp. 1782–1790, Dec. 2008.
- [13] W. Xu, M. H. Jericho, I. A. Meinertzhagen, and H. J. Kreuzer, "Digital in-line holography for biological applications," *Proc. Nat. Acad. Sci.*, vol. 98, no. 20, pp. 11301–11305, 2001.
- [14] I. Moon, M. Daneshpanah, B. Javidi, and A. Stern, "Automated three-dimensional identification and tracking of micro/nanobiological organisms by computational holographic microscopy," *Proc. IEEE*, vol. 97, no. 6, pp. 990–1010, Jun. 2009.
- [15] B. Javidi, M. Daneshpanah, and I. Moon, "Three-dimensional holographic imaging for identification of biological micro/nanoorganisms," *IEEE Photon. J.*, vol. 2, no. 2, pp. 256–259, Apr. 2010.
- [16] I. Moon, F. Yi, and B. Javidi, "Automated three-dimensional microbial sensing and recognition using digital holography and statistical sampling," *Sensors*, vol. 10, no. 9, pp. 8437–8451, 2010.
- [17] W. Bishara, T.-W. Su, A. F. Coskun, and A. Ozcan, "Lensfree on-chip microscopy over a wide field-of-view using pixel super-resolution," *Opt. Exp.*, vol. 18, no. 11, pp. 11181–11191, 2010.
- [18] I. Moon, M. Daneshpanah, A. Anand, and B. Javidi, "Cell identification computational 3-D holographic microscopy," *Opt. Photon. News*, vol. 22, no. 6, pp. 18–23, 2011.
- [19] Y. Rivenson, A. Stern, and B. Javidi, "Improved depth resolution by single-exposure in-line compressive holography," *Appl. Opt.*, vol. 52, no. 1, pp. A223–A231, 2013.
- [20] E. Cucho, P. Marquet, and C. Depeursinge, "Simultaneous amplitude-contrast and quantitative phase-contrast microscopy by numerical reconstruction of Fresnel off-axis holograms," *Appl. Opt.*, vol. 38, no. 34, pp. 6994–7001, 1999.
- [21] E. Cucho, F. Bevilacqua, and C. Depeursinge, "Digital holography for quantitative phase-contrast imaging," *Opt. Lett.*, vol. 24, no. 5, pp. 291–294, 1999.
- [22] E. Cucho, P. Marquet, and C. Depeursinge, "Spatial filtering for zero-order and twin-image elimination in digital off-axis holography," *Appl. Opt.*, vol. 39, no. 23, pp. 4070–4075, 2000.
- [23] P. Marquet et al., "Digital holographic microscopy: A noninvasive contrast imaging technique allowing quantitative visualization of living cells with subwavelength axial accuracy," *Opt. Lett.*, vol. 30, no. 5, pp. 468–470, 2005.
- [24] S. De Nicola, A. Finizio, G. Pierattini, P. Ferraro, and D. Alfieri, "Angular spectrum method with correction of anamorphism for numerical reconstruction of digital holograms on tilted planes," *Opt. Exp.*, vol. 13, no. 24, pp. 9935–9940, 2005.
- [25] F. Charrière et al., "Cell refractive index tomography by digital holographic microscopy," *Opt. Lett.*, vol. 31, no. 2, pp. 178–180, 2006.
- [26] F. Dubois et al., "Digital holographic microscopy for the three-dimensional dynamic analysis of *in vitro* cancer cell migration," *J. Biomed. Opt.*, vol. 11, no. 5, p. 054032, 2006.
- [27] T. Colomb et al., "Automatic procedure for aberration compensation in digital holographic microscopy and applications to specimen shape compensation," *Appl. Opt.*, vol. 45, no. 5, pp. 851–863, 2006.
- [28] L. Miccio et al., "Direct full compensation of the aberrations in quantitative phase microscopy of thin objects by a single digital hologram," *Appl. Phys. Lett.*, vol. 90, no. 4, p. 041104, 2007.
- [29] G. Pedrini, F. Zhang, and W. Osten, "Digital holographic microscopy in the deep (193 nm) ultraviolet," *Appl. Opt.*, vol. 46, no. 32, pp. 7829–7835, 2007.
- [30] B. Kemper and G. von Bally, "Digital holographic microscopy for live cell applications and technical inspection," *Appl. Opt.*, vol. 47, no. 4, pp. A52–A61, 2008.
- [31] B. Rappaz et al., "Comparative study of human erythrocytes by digital holographic microscopy, confocal microscopy, and impedance volume analyzer," *Cytometry A*, vol. 73A, no. 10, pp. 895–903, Oct. 2008.
- [32] B. Rappaz et al., "Noninvasive characterization of the fission yeast cell cycle by monitoring dry mass with digital holographic microscopy," *J. Biomed. Opt.*, vol. 14, no. 3, pp. 034045–034049, 2009.
- [33] A. Faridian, D. Hopp, G. Pedrini, U. Eigenthaler, M. Hirscher, and W. Osten, "Nanoscale imaging using deep ultraviolet digital holographic microscopy," *Opt. Exp.*, vol. 18, no. 13, pp. 14159–14164, 2010.
- [34] A. Anand, V. K. Chhaniwal, and B. Javidi, "Real-time digital holographic microscopy for phase contrast 3D imaging of dynamic phenomena," *J. Display Technol.*, vol. 6, no. 10, pp. 500–505, 2010.
- [35] D. Shin, M. Daneshpanah, A. Anand, and B. Javidi, "Optofluidic system for three-dimensional sensing and identification of micro-organisms with digital holographic microscopy," *Opt. Lett.*, vol. 35, no. 23, pp. 4066–4068, 2010.
- [36] B. Kemper et al., "Label-free quantitative cell division monitoring of endothelial cells by digital holographic microscopy," *J. Biomed. Opt.*, vol. 15, no. 3, p. 036009, 2010.
- [37] N. T. Shaked, L. L. Satterwhite, A. Wax, and N. Bursac, "Whole-cell-analysis of live cardiomyocytes using wide-field interferometric phase microscopy," *Biomed. Opt. Exp.*, vol. 1, no. 2, pp. 706–719, 2010.
- [38] A. Anand, V. K. Chhaniwal, and B. Javidi, "Imaging embryonic stem cell dynamics using quantitative 3D digital holographic microscopy," *IEEE Photon. J.*, vol. 3, no. 3, pp. 546–554, Jun. 2011.
- [39] F. Dubois and C. Yourassowsky, "Full off-axis red-green-blue digital holographic microscope with LED illumination," *Opt. Lett.*, vol. 37, no. 12, pp. 2190–2192, 2012.
- [40] A. Anand, V. K. Chhaniwal, N. R. Patel, and B. Javidi, "Automatic identification of malaria-infected RBC with digital holographic microscopy using correlation algorithms," *IEEE Photon. J.*, vol. 4, no. 5, pp. 1456–1464, Oct. 2012.
- [41] I. Moon, B. Javidi, F. Yi, D. Boss, and P. Marquet, "Automated statistical quantification of three-dimensional morphology and mean corpuscular hemoglobin of multiple red blood cells," *Opt. Exp.*, vol. 20, no. 9, pp. 10295–10309, 2012.
- [42] F. Yi, I. Moon, B. Javidi, D. Boss, and P. Marquet, "Automated segmentation of multiple red blood cells with digital holographic microscopy," *J. Biomed. Opt.*, vol. 18, no. 2, p. 026006, 2013.
- [43] I. Moon, F. Yi, Y. H. Lee, B. Javidi, D. Boss, and P. Marquet, "Automated quantitative analysis of 3D morphology and mean corpuscular hemoglobin in human red blood cells stored in different periods," *Opt. Exp.*, vol. 21, no. 25, pp. 30947–30957, 2013.
- [44] V. Mico, C. Ferreira, Z. Zalevsky, and J. García, "Spatially-multiplexed interferometric microscopy (SMIM): Converting a standard microscope into a holographic one," *Opt. Exp.*, vol. 22, no. 12, pp. 14929–14943, 2014.
- [45] R. Liu, A. Anand, D. K. Dey, and B. Javidi, "Entropy-based clustering of embryonic stem cells using digital holographic microscopy," *J. Opt. Soc. Amer. A*, vol. 31, no. 4, pp. 677–684, 2014.
- [46] A. Anand and B. Javidi, "Digital holographic microscopy for automated 3D cell identification: An overview," *Chin. Opt. Lett.*, vol. 12, no. 6, p. 060012, 2014.
- [47] B. Rappaz, I. Moon, F. Yi, B. Javidi, P. Marquet, and G. Turcatti, "Automated multi-parameter measurement of cardiomyocytes dynamics with digital holographic microscopy," *Opt. Exp.*, vol. 23, no. 10, pp. 13333–13347, 2015.
- [48] N. R. Patel, V. K. Chhaniwal, B. Javidi, and A. Anand, "Identification of malaria infected red blood samples by digital holographic quantitative phase microscope," *Proc. SPIE*, vol. 9536, p. 95360E, Jun. 2015.

- [49] F. Yi, I. Moon, and B. Javidi, "Cell morphology-based classification of red blood cells using holographic imaging informatics," *Biomed. Opt. Exp.*, vol. 7, no. 6, pp. 2385–2399, 2016.
- [50] N. T. Shaked, "Quantitative phase microscopy of biological samples using a portable interferometer," *Opt. Lett.*, vol. 37, no. 11, pp. 2016–2018, 2012.
- [51] M. Mir, K. Tangella, and G. Popescu, "Blood testing at the single cell level using quantitative phase and amplitude microscopy," *Biomed. Opt. Exp.*, vol. 2, no. 12, pp. 3259–3266, 2011.
- [52] A. Anand et al., "Single beam Fourier transform digital holographic quantitative phase microscopy," *App. Phys. Lett.*, vol. 103, no. 10, p. 103705, 2014.
- [53] Y. Park et al., "Refractive index maps and membrane dynamics of human red blood cells parasitized by plasmodium falciparum," *Proc. Nat. Acad. Sci.*, vol. 105, no. 37, pp. 13730–13735, 2008.
- [54] S. Mahajan, V. Trivedi, P. Vora, V. Chhaniwal, B. Javidi, and A. Anand, "Highly stable digital holographic microscope using Sagnac interferometer," *Opt. Lett.*, vol. 40, no. 16, pp. 3743–3746, 2015.
- [55] B. Kemper, A. Vollmer, C. E. Rommel, J. Schnekenburger, and G. von Bally, "Simplified approach for quantitative digital holographic phase contrast imaging of living cells," *J. Biomed. Opt.*, vol. 16, no. 2, p. 026014, 2011.
- [56] A. S. G. Singh, A. Anand, R. A. Leitgeb, and B. Javidi, "Lateral shearing digital holographic imaging of small biological specimens," *Opt. Exp.*, vol. 20, no. 21, pp. 23617–23622, 2012.
- [57] V. K. Chhaniwal, A. S. G. Singh, R. Leitgeb, B. Javidi, and A. Anand, "Quantitative phase-contrast imaging with compact digital holographic microscope employing Lloyd's mirror," *Opt. Lett.*, vol. 37, no. 24, pp. 1527–1529, 2012.
- [58] A. Anand et al., "Compact, common path quantitative phase microscopic techniques for imaging cell dynamics," *Pramana*, vol. 82, no. 1, pp. 71–78, 2014.
- [59] S. Ebrahimi, A. R. Moradi, A. Anand, and B. Javidi, "Digital holographic microscopy with coupled optical fiber trap for cell measurement and manipulation," *Opt. Lett.*, vol. 39, no. 10, pp. 2916–2919, 2014.
- [60] D. Roitshtain, N. A. Turko, B. Javidi, and N. T. Shaked, "Flipping interferometry and its application for quantitative phase microscopy in a micro-channel," *Opt. Lett.*, vol. 41, no. 10, pp. 2354–2357, 2016.
- [61] T. Kreis, *Handbook of Holographic Interferometry*. Weinheim, Germany: Wiley, 2005.
- [62] U. Schnars and W. Jueptner, *Digital Holography: Digital Hologram Recording, Numerical Reconstruction and Related Techniques*. Berlin, Germany: Springer, 2005.
- [63] J. W. Goodman, *Introduction to Fourier Optics*. New York, NY, USA: McGraw-Hill, 1996.
- [64] P. Ferraro, S. De Nicola, G. Coppola, A. Finizio, D. Alfieri, and G. Pierattini, "Controlling image size as a function of distance and wavelength in Fresnel-transform reconstruction of digital holograms," *Opt. Lett.*, vol. 29, no. 8, pp. 854–856, 2004.
- [65] M. Wojdyla, S. Raj, and D. Petrov, "Absorption spectroscopy of single red blood cells in the presence of mechanical deformations induced by optical traps," *J. Biomed. Opt.*, vol. 17, no. 9, p. 097006, Sep. 2012.
- [66] R. Card, "Red cell membrane changes during storage," *Transfus. Med. Rev.*, vol. 2, no. 1, pp. 40–47, 1988.
- [67] D. J. Kor, C. M. van Buskirk, and O. Gajic, "Red blood cell storage lesion," *Bosn. J. Basic Med. Sci.*, vol. 9, pp. 21–27, Oct. 2009.
- [68] M. Hammer, D. Schweitzer, B. Michel, E. Thamm, and A. Kolb, "Single scattering by red blood cells," *Appl. Opt.*, vol. 37, no. 31, pp. 7410–7418, 1998.
- [69] R. Barer, "Interference microscopy and mass determination," *Nature*, vol. 169, no. 4296, pp. 366–367, 1952.
- [70] G. Lim, M. Wortis, and R. Mukhopadhyay, "Stomatocyte–discocyte–echinocyte sequence of the human red blood cell: Evidence for the bilayer–couple hypothesis from membrane mechanics," *Proc. Nat. Acad. Sci.*, vol. 99, no. 26, pp. 16766–16769, 2002.
- [71] N. Mukhopadhyay, *Probability and Statistical Inference*. New York, NY, USA: Marcel Dekker, 2000.
- [72] T. S. Lee, "Image representation using 2D Gabor wavelets," *IEEE Trans. Pattern Anal. Mach. Intell.*, vol. 18, no. 10, pp. 959–971, Oct. 1996.
- [73] D. Zhang, M. M. Islam, G. Lu, and I. J. Sumana, "Rotation invariant curvelet features for region based image retrieval," *Int. J. Comput. Vis.*, vol. 98, no. 2, pp. 187–201, Oct. 2012. [Online]. Available: <http://link.springer.com/10.1007/s11263-011-0503-6>
- [74] R. C. Gonzalez and R. E. Woods, *Digital Image Processing*. New York, NY, USA: Prentice-Hall, 2002.
- [75] A. Rencher, *Methods of Multivariate Analysis*. New York, NY, USA: Wiley, 2002.
- [76] E. Gose, *Pattern Recognition and Image Analysis*. New Jersey, NJ, USA: Prentice-Hall, 1997.
- [77] A. Trampuz, M. Jereb, I. Muzlovic, and R. M. Prabhu, "Clinical review: Severe malaria," *Critical Care*, vol. 7, no. 4, pp. 315–323, 2003.
- [78] P. Girshovitz and N. T. Shaked, "Generalized cell morphological parameters based on interferometric phase microscopy and their application to cell life cycle characterization," *Biomed. Opt. Exp.*, vol. 3, no. 8, pp. 1757–1773, 2012.
- [79] Y. A. Abassi et al., "Dynamic monitoring of beating periodicity of stem cell-derived cardiomyocytes as a predictive tool for preclinical safety assessment," *Brit. J. Pharmacol.*, vol. 165, no. 5, pp. 1424–1441, 2012.
- [80] C. Carlson et al., "Phenotypic screening with human iPSC cell-derived cardiomyocytes HTS-compatible assays for interrogating cardiac hypertrophy," *J. Biomolecular Screening*, vol. 18, pp. 1203–1211, Sep. 2013.
- [81] W. E. Moerner and D. P. Fromm, "Methods of single-molecule fluorescence spectroscopy and microscopy," *Rev. Sci. Instrum.*, vol. 74, no. 8, pp. 3597–3619, 2003.
- [82] M. Strojnik, G. Paez, and M. Mantravadi, "Lateral shear interferometers," in *Optical Shop Testing*, 3rd ed. New Jersey, NJ, USA: Wiley, 2007, pp. 122–184.
- [83] G. Popescu, K. Badizadegan, R. R. Dasari, and M. S. Feld, "Observation of dynamic subdomains in red blood cells," *J. Biomed. Opt.*, vol. 11, no. 5, pp. 040503-1–040503-3, Jul. 2006.
- [84] B. Javidi, S. Rawat, S. Komatsu, and A. Markman, "Cell identification using single beam lensless imaging with pseudo-random phase encoding," *Opt. Lett.*, vol. 41, no. 15, pp. 3663–3666, 2016.
- [85] I. Moon, A. Anand, M. Cruz, and B. Javidi, "Identification of malaria-infected red blood cells via digital shearing interferometry and statistical inference," *IEEE Photon. J.*, vol. 5, no. 5, pp. 6900207-1–6900207-7, Oct. 2013.
- [86] S. Rawat, S. Komatsu, A. Markman, A. Anand, and B. Javidi, "Compact and field portable 3D printed shearing digital holographic microscope for automated cell identification," *Appl. Opt.*, vol. 56, 2017.
- [87] H. S. Park, M. T. Rinehart, K. A. Walzer, J.-T. A. Chi, and A. Wax, "Automated detection of *P. Falciparum* using machine learning algorithms with quantitative phase images of unstained cells," *PLoS ONE*, vol. 11, no. 9, p. e0163045, 2016, doi: 10.1371/journal.pone.0163045.
- [88] J. C. Contreras-Naranjo, Q. Wei, and A. Ozcan, "Mobile phone-based microscopy, sensing, and diagnostics," *IEEE J. Sel. Topics Quantum Electron.*, vol. 22, no. 3, May 2016, Art. no. 7100414, doi: 10.1109/JSTQE.2015.2478657.
- [89] A. El Mallahi, C. Minetti, and F. Dubois, "Automated three-dimensional detection and classification of living organisms using digital holographic microscopy with partial spatial coherent source: Application to the monitoring of drinking water resources," *Appl. Opt.*, vol. 52, no. 1, pp. A68–A80, 2013.
- [90] P. Memmolo et al., "Identification of bovine sperm head for morphometry analysis in quantitative phase-contrast holographic microscopy," *Opt. Exp.*, vol. 19, no. 23, pp. 23215–23226, 2011.

ABOUT THE GUEST EDITORS

Arun Anand received the Ph.D. degree in applied physics from the M. S. University of Baroda, India, in 2003.

From 2002 to 2008, he worked as a Scientist at the Institute for Plasma Research, Gandhinagar, India. Presently he is a faculty member at Applied Physics Department at the M. S. University of Baroda. He has more than 100 publications including peer-reviewed journal articles, conference proceedings and invited conference papers. His research interests include 3-D microscopes for cell imaging and identification, biomedical optical systems, digital holography and optical instrumentation.



Inkyu Moon (Member, IEEE) received the B.S. degree in electronics engineering from SungKyunkwan University, South Korea, in 1996 and the Ph.D. degree in electrical and computer engineering from the University of Connecticut, Storrs, CT, USA, in 2007.

He joined Chosun University in Korea in 2009. He is currently a Professor at the School of Computer Engineering. He is Director of the Center for Holographic Imaging Informatics, Chosun University. His research interests include digital holography, biomedical imaging, biomedical informatics and optical information processing.

Dr. Moon is a member of OSA and SPIE.

Bahram Javidi (Fellow, IEEE) received the B.S. degree from George Washington University, Washington, DC, USA, and the M.S. and Ph.D. degrees from the Pennsylvania State University, University Park, PA, USA, all in electrical engineering.

He is the Board of Trustees Distinguished Professor at the University of Connecticut, Storrs, CT, USA. He has over 1000 publications, including nearly 450 peer reviewed journal articles, over 450 conference proceedings, including over 120 Plenary Addresses, Keynote Addresses, and invited conference papers. His papers have been cited 33000 times according to the Google Scholar Citations (h -index=85, $i10$ -index=537). He is a coauthor on nine Best Paper Awards.



Prof. Javidi received the Quantum Electronics and Optics Prize for Applied Aspects by the European Physical Society in June 2015. He has been named Fellow of several scientific societies, including IEEE, OSA, and SPIE. In 2010, he was the recipient of The George Washington University's Distinguished Alumni Scholar Award, University's highest honor for its alumni in all disciplines. In 2008, he received a Fellow award by John Simon Guggenheim Foundation. He received the 2008 IEEE Donald G. Fink prized paper award among all (over 150) IEEE Transactions, Journals, and Magazines. In 2007, The Alexander von Humboldt Foundation awarded Prof. Javidi with the Humboldt Prize for outstanding U.S. Scientists. He received the Technology Achievement Award from the SPIE in 2008. In 2005, he received the Dennis Gabor Award in Diffractive Wave Technologies from SPIE. He was the recipient of the IEEE Photonics Distinguished Lecturer Award twice in 2003/2004 and 2004/2005. He was awarded the IEEE Best Journal Paper Award from IEEE TRANSACTIONS ON VEHICULAR TECHNOLOGY twice in 2002 and 2005. Early in his career, the National Science Foundation named him a Presidential Young Investigator and he received The Engineering Foundation and the IEEE Faculty Initiation Award. He was selected in 2003 as one of the nation's top 160 engineers between the ages of 30 to 45 by the National Academy of Engineering (NAE) to be an invited speaker at The Frontiers of Engineering Conference which was co-sponsored by The Alexander von Humboldt Foundation. He is an alumnus of the Frontiers of Engineering of The National Academy of Engineering since 2003. He has served on the Editorial Board of the PROCEEDINGS OF THE IEEE (ranked #1 among all electrical engineering journals), the advisory board of the IEEE PHOTONICS JOURNAL, and he was on the founding board of editors of IEEE/OSA JOURNAL OF DISPLAY TECHNOLOGY.